Applied Ocean Research 89 (2019) 96–114

Contents lists available at ScienceDirect

Applied Ocean Research

journal homepage: www.elsevier.com/locate/apor

Dynamic response of a monopile wind turbine in waves: Experimental uncertainty analysis for validation of numerical tools

Erin Bachynski[a,*], Maxime Thys[b], Virgile Delhaye[c]

[a] NTNU, Department of Marine Technology, 7491 Trondheim, Norway
[b] SINTEF Ocean, 7450 Trondheim, Norway
[c] SINTEF Industri, 7465 Trondheim, Norway

ARTICLE INFO

Keywords:
Ringing
Higher order wave loads
Hydrodynamic model testing
Monopile
Offshore wind turbine
Uncertainty

ABSTRACT

The responses of a monopile offshore wind turbine subjected to irregular wave loads are investigated numerically and experimentally, considering a range of sea states. An extensive experimental campaign was carried out on a fully flexible model, representative of a 5 MW offshore wind turbine, at 1:40 scale. An assessment of the experimental results for the response amplitude operator for regular waves and the 90th percentile seabed bending moment in long-crested irregular waves is carried out using two models (analytical and numerical) for uncertainty propagation, suggesting that bias errors in the model properties and in the wave elevation contribute the most to the total uncertainty. The experimental results are also compared to a numerical model using beam elements and Morison-type wave loads with second order wave kinematics. The numerical model does not capture all of the responses within the level of uncertainty of the experiments, and possible reasons for the discrepancies are discussed.

1. Introduction

The offshore wind industry is moving towards larger turbines in order to save costs on installation and maintenance. The increase in rotor size and aerodynamic loads requires increasingly large support structures. For monopile wind turbine foundations (which support roughly 80% of the offshore wind turbines in Europe [1]), this corresponds to an increase in diameter, and more significant wave loads. Furthermore, to maintain a soft-stiff design with respect to 1p (rotor frequency) and 3p (blade sweeping) excitation, the decrease in rotor speed associated with upscaling also leads to a reduction in the first global bending natural frequency of large monopile wind turbines. As a result, the ocean waves whose second, third or fourth harmonic are capable of exciting the structure at its natural frequency, are waves with lower periods - and (for typical severe sea states) larger energy. In severe weather conditions, when the turbine is typically parked with the blades feathered, monopile wind turbines are very lightly damped and therefore particularly sensitive to wave loads which excite resonant responses.

In order to ensure safe yet economical design of large monopile wind turbines, the hydrodynamic loads and the ringing-type responses need to be predicted accurately. Here, we apply Faltinsen's definition of ringing: “transient structural deflections at frequencies substantially higher than the incident wave frequencies” [2]. Ringing-type responses were extensively studied experimentally and theoretically in the 1990s in support of the development of tension leg platforms and gravity-based structures for the oil and gas industry [2–8]. For shallower water and irregular waves, state-of-the-art methods include using (modified) Morison's equation with 2nd order irregular wave kinematics [9], Morison's equation or Rainey's equation combined with wave kinematics from nonlinear potential theory or from CFD [10–12], or wave kinematics from embedded stream function or higher order Stokes waves [13]. Recently, Kristiansen and Faltinsen introduced a new load model for intermediate water depth which can be applied to monopile wind turbines [14]. Compared to experiments with a rigid monopile and regular waves, the new load model shows good agreement in the third order load for small to medium wave steepness. Loads from breaking waves require the inclusion of additional load models [15]. In the present work, a Morison-type load model – typical for engineering calculations – is selected for simplicity and in order to establish a baseline comparison for further work.

Model scale experiments are used to provide validation data for different numerical approaches; several recent relevant model tests are summarized in [9]. Previous tests include rigid [9,11,14,15–17], single-mode [9,18], and fully flexible models [11,19,20]. While rigid models can provide important information about the wave loads, the response

* Corresponding author.
E-mail address: erin.bachynski@ntnu.no (E. Bachynski).

https://doi.org/10.1016/j.apor.2019.05.002
Received 13 August 2018; Received in revised form 5 April 2019; Accepted 4 May 2019
Available online 23 May 2019

of the structure is what really drives design. A single-mode (pitching) model is simple to build, but doesn't completely match the deformations of the structure in the model compared to full scale. As a result, radiation loads may be too large at model scale compared to full scale, and the response to wave excitation may not correctly represent the full scale responses. Furthermore, the second mode may be of importance, especially for breaking waves [20]. Here, we present a new set of experiments, which were carried out with a highly instrumented model at 1:40 scale in the Ocean Basin at SINTEF Ocean in August 2017. The model consisted of a fully flexible monopile with a mass representing the rotor-nacelle assembly. The first two modes of a prototype design were represented with reasonable accuracy and the model was subjected to a range of regular (long-crested) and irregular (long- and short-crested) waves.

In order to use experimental data for validation of numerical tools, there is a need for thorough uncertainty analysis regarding the hydrodynamic experiments as well as the numerical models themselves [21]. The present test program included repetition tests as well as multiple realizations of the same wave conditions, such that the statistical variations can be investigated. This paper presents an estimation of the uncertainty in the experiments, focusing on the long-crested wave conditions, as well as a comparison of the results with state-of-the-art engineering models. Repeatability is assessed directly from the experimental results, and possible bias errors are estimated and propagated to the responses of interest using a simple semi-analytical model and using a state-of-the-art engineering model.

The main focus of the present paper is to identify the level of uncertainty in the experimental results, in order to understand whether or not the discrepancy between the numerical models and the experimental results is within the experimental uncertainty. Many experimental results have been presented in this area - with very little discussion of the level of certainty in the results. This work attempts to shed light on the level of uncertainty in the estimation of extrema, and to show the extent to which engineering methods can reproduce the 90th percentile responses within the experimental uncertainty.

Section 2 presents the experimental setup and test campaign, while Section 3 explains the numerical model. An assessment of the uncertainty in the experimental campaign is given in Section 4. Results of the experimental campaign and numerical analyses are presented together in Section 5, focusing on the ability of the numerical model to capture selected response metrics within the estimated experimental uncertainty. Differences between the numerical model and experimental results are also examined.

2. Experimental setup

2.1. Model and instrumentation

The experimental model represents a prototype 5 MW offshore wind turbine with a monopile support structure in 30 m water depth. The model tests were carried out at scale 1:40 in the Ocean Basin at SINTEF Ocean. Unless otherwise noted, physical quantities are reported at full scale. Froude scaling (including the difference between the fresh water density in the model tests and sea water density at full scale) is applied in order to scale the model test results. Since the monopile wave loads are dominated by inertia-type loads, the error induced by the difference in Reynolds number at model scale compared to full scale is assumed to be small.

The prototype design corresponds to the NREL 5 MW reference wind turbine [22] supported by the offshore tower developed in OC3 Phase III [23] and a 7 m diameter monopile, with the OC3 Phase II soil stiffness parameters [24]. For the prototype design, the monopile thickness is 60 mm and the transition from monopile to tower occurs at 10 m above the waterline. For the model scale design, as shown in Fig. 1, a flexible backbone from the top of the tower to the seabed provides the correct distribution of bending stiffness, while outer shells

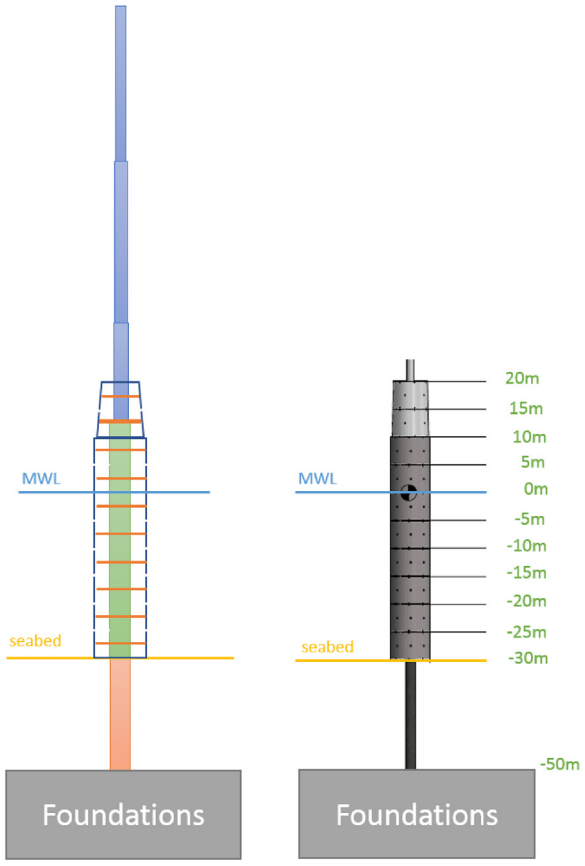

Fig. 1. Sketch of the monopile model, without (left) and with (right) outer shells.

placed around the backbone provide the correct outer diameter in the wetted section of the monopile. The outer shells, in 5 m sections, are connected to the backbone at the vertical center of each section. The space between the inner backbone and the outer shells is filled with divinycell in order to avoid sloshing water in the monopile. At the seabed, the monopile is connected to a 50 m long "soil spring": a pipe section which extends down to the foundation and which was designed to give a representative bending stiffness for the monopile and soil.

The mass distribution of the model, including the instrumentation, does not precisely follow the mass distribution of the prototype 5 MW design, but provides a reasonable approximation. At the top of the model, as shown in Fig. 2, two aerodynamic drag disks were installed. These disks, which were installed in an attempt to increase the aerodynamic damping of the system, match the mass of the rotor-nacelle assembly (RNA). The inertia provided by these disks is, however, larger than that of the prototype RNA, and there is no equivalent flexibility representing the wind turbine blades, both of which can influence the second and third eigenmodes. A detailed comparison of the natural frequencies is given in Section 5.2 (Table 1).

The model is instrumented with strain gauges at 20 elevations (ranging from $z = -46.00$ m to $z = 16.90$ m). At each instrumented elevation, there are 4 strain gauges in order to measure bending moments about the x- and y- axes. Since the wave loads are transferred to the center core of the model only at horizontal connection plates, the shear forces (derived from the bending moments) are nearly constant from the middle of one section to the middle of the next. In addition to the strain gauges, 10 accelerometers were installed on the model. These are used for extracting the mode shapes and can also be used for estimating the wave loads via i.e. force identification techniques [25].

Wave gauges were installed in the basin during both calibration and testing with the model. Fig. 3 shows the wave gauge positions during

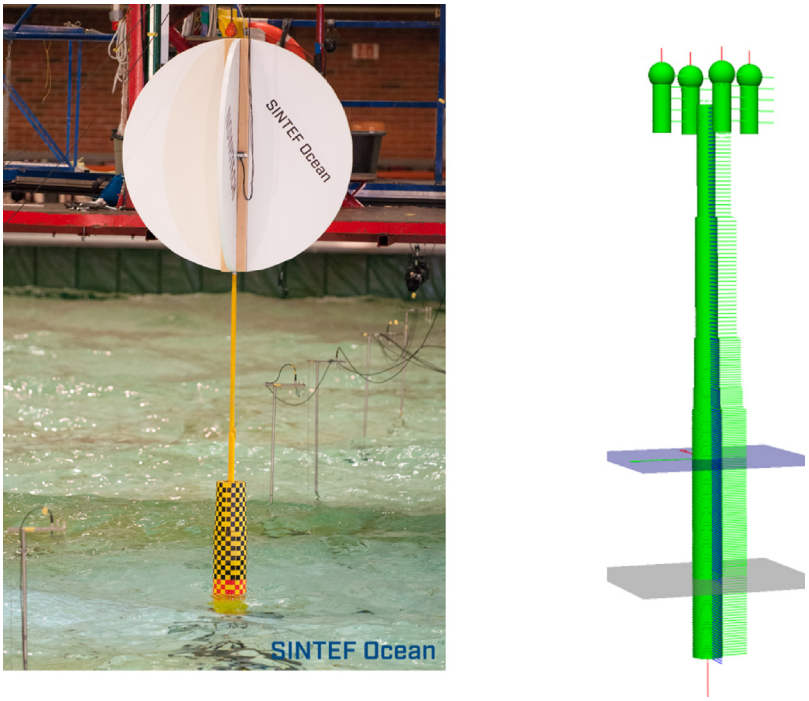

Fig. 2. Left: photograph of the model installed in the wave basin, highlighting the drag disk. Right: numerical model in SIMA, where the four upper lines represent the drag disk. Transition from red to black checkerboard indicates the calm water free surface elevation.

calibration of long-crested waves. There were 13 standing probes (present during both calibration and tests with the model) and 23 probes along a wave harp (a set of tightly-spaced wave probes aligned with the wave propagation direction, with a distance of 6 m between each probe and connected to a single support) which was only present during wave calibration. The wave harp is shown in Fig. 4.

2.2. Test matrix

As shown in Table 2, 19 regular waves were tested, with periods (T) ranging from 6 to 15 seconds. Two steepness values were considered (approximately 1/30 and approximately 1/40). These different steepnesses can be useful for identifying nonlinear loads and behaviors. In Table 2, the Keulegan-Carpenter (KC) number for regular waves is calculated based on the maximum velocity according to linear theory, that is:

$$\mathrm{KC} = \frac{\pi H_1}{\tanh(\mathrm{kh})D}, \tag{1}$$

where k is the wave number, h is the water depth, and D is the diameter. The Ursell (Ur) number in Table 2 is calculated using the linear wave height (H_1) and the wavelength λ according to the linear dispersion relationship:

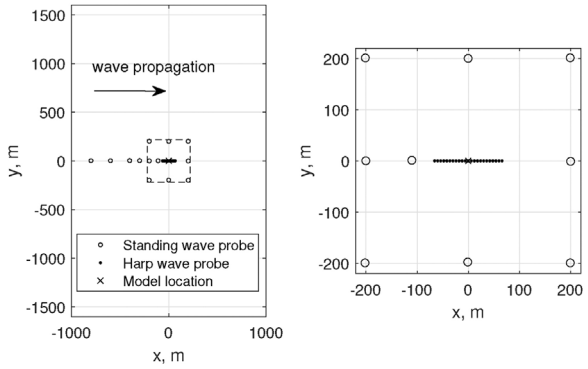

Fig. 3. Wave probe layout during calibration of long-crested waves. Left: full basin extents, dashed lines show zoom area. Right: zoom near the model, showing the tightly-spaced wave probes in the harp.

$$\mathrm{Ur} = \frac{H_1 \lambda^2}{h^3}. \tag{2}$$

As shown in Table 2, the KC number for all of the considered tests is quite low. For the smallest waves ($KC < 1.25$), no flow separation is expected [26], and for KC up to 5.0, the added mass coefficient is not expected to vary significantly [27].

Table 1
Key model particulars, compared to the design prototype and to the OC3 Phase II monopile [24]. All values in full scale. Note that the OC3 Phase II monopile is in 20 m water depth, compared to the present model in 30 m water depth.

	Model Tests	Prototype	OC3 Phase II Monopile [24]
Diameter (wetted section of monopile) [m]	7.0	7.0	6.0
Tower base diameter (10 m above waterline) [m]	6.5	6.5	6.0
Tower top diameter [m]	3.87	3.87	3.87
RNA mass [tonnes]	335.9	350.0	350.0
RNA Ixx about RNA CoG [tonnes-m^2]	7.136x10^4	4.00x10^4	4.00x10^4
RNA Iyy about RNA CoG [tonnes-m^2]	7.136x10^4	3.07x10^4	3.07x10^4
RNA Izz about RNA CoG [tonnes-m^2]	9.513x10^4	2.44x10^4	2.44x10^4
Monopile penetration depth (below seabed)	-	46 m	30 m

Fig. 4. Wave harp as installed during wave calibration.

Table 2
Regular wave tests.

H (m)	T (s)	KC	Ur	Repetitions
1.9	6.0	0.85	0.22	0
2.6	7.0	1.18	0.55	0
3.3	8.0	1.54	1.13	0
4.2	9.0	2.04	2.12	0
5.2	10.0	2.65	3.63	0
6.3	11.0	3.39	5.78	0
7.5	12.0	4.27	8.71	1
8.8	13.0	5.31	12.57	0
10.2	14.0	6.50	17.53	1
1.4	6.0	0.63	0.16	0
1.9	7.0	0.86	0.40	0
2.5	8.0	1.17	0.85	0
3.2	9.0	1.55	1.62	0
3.9	10.0	1.99	2.72	0
4.7	11.0	2.53	4.31	0
5.6	12.0	3.19	6.50	0
6.6	13.0	3.98	9.43	0
7.7	14.0	4.91	13.23	1
8.8	15.0	5.92	17.88	0

Table 3
Long-crested irregular wave tests.

H_s (m)	T_p (s)	γ	KC	Ur	Additional seeds	Repetitions (seed 1)
1.9	6	5	0.85	0.01	3	0
3.4	8	2.1	1.53	0.03	0	0
4.6	9	2.5	2.06	0.05	3	0
6.5	9	5	2.92	0.07	0	0
8	9	5	3.59	0.08	0	0
8.1	10	5	3.64	0.10	0	0
8.5	11	4.1	3.81	0.12	0	0
9	12.3	2.8	4.04	0.15	3	8
8.5	13	1.9	3.81	0.15	0	0

In addition to the regular wave tests, 56 three-hour duration (28 long-crested and 28 short-crested) irregular sea states were tested. The short-crested wave conditions are not studied in the present work, while the long-crested wave conditions are shown in Table 3.

The wave conditions in Table 3 are also characterized by a representative KC number using the formulation given in DNV-OS-J101 [28] and irregular Ursell number (Ur) [29]. The representative KC number is calculated as:

$$\mathrm{KC} = \frac{\pi H_s}{D}, \tag{3}$$

where D is the diameter and H_s the characteristic wave amplitude. The irregular Ursell number is computed as [29]:

$$\mathrm{Ur} = \frac{k_p H_s}{2(k_p h)^2}, \tag{4}$$

where k_p is the wave number at the peak frequency and h the water depth. The maximum Ursell value computed is 0.15, below the validity limit for second order waves (Ur = 0.33) where one begins to observe artificial bumps [30]. Similar to the regular waves, the KC number is low for all of the irregular wave tests.

3. Numerical modelling

A numerical model of the test set-up is developed at full scale in the SIMA software, using the RIFLEX finite element program from SINTEF Ocean. The numerical model consists of beam elements, following the discretization in Table 4, which are subjected to hydrodynamic loads. The bottom of the soil spring is modelled as fully fixed, while the top of the structure is free.

The hydrodynamic loading in the numerical model is based on a modified Morison model, applied to each strip of the monopile. For a circular cylinder in long-crested waves, the distributed component of the force proposed by Kristiansen and Faltinsen (KF) [14] or the distributed force from Manners and Rainey [31] can be expressed as:

$$\mathrm{d}F_h = \rho\pi\frac{D^2}{4}\mathrm{d}z a_{h1} + \rho\pi\frac{D^2}{4}\mathrm{d}z C_a(a_{h2} - \ddot{x}), \tag{5}$$

with:

$$a_{h1} = \frac{\partial u}{\partial t} + u\frac{\partial u}{\partial x} + w\frac{\partial u}{\partial z} \tag{6}$$

$$a_{h2} = \frac{\partial u}{\partial t} + w\frac{\partial u}{\partial z} \tag{7}$$

(the transverse velocity v is zero for long-crested waves, while the horizontal, u, and vertical, w, components are nonzero). Furthermore, in Eq. (5), ρ is the density of water, D is the diameter of a vertical strip of the monopile, and C_a (taken here to be 1.0) is the so-called mass coefficient. The structural acceleration is $\ddot{x}$. The two terms on the right hand side are usually referred to as the inertia terms. For practical reasons, the existing formulation in the RIFLEX software requires using the same wave particle acceleration in both terms. Three formulations of the load are included here:

1) approach a_1, the total acceleration including all advective terms. This model corresponds to the R2 model in [9], except that viscous drag forces are neglected in the present work.

$$a_{h1} = a_{h2} = \frac{\partial u}{\partial t} + u\frac{\partial u}{\partial x} + w\frac{\partial u}{\partial z}. \tag{8}$$

Table 4
Structural modelling. *The mass of the drag disk is modelled through rigid elements connected to these beam elements.

Line type	Length (m)	Number of elements	Cross-section properties
Soil spring	20	20	D = 7 m, E = 3312 GPa
Wetted part of monopile	30	70	D = 7 m, E = 3312 GPa
Tower	87	20	D = 7 m to D = 4.3 m, E = 3312 GPa
Drag disk	7	5	D = 4.3 m, rigid, no mass*

2) approach a_2, a formulation without the $u\frac{\partial u}{\partial x}$ term:

$$a_{h1} = a_{h2} = \frac{\partial u}{\partial t} + w\frac{\partial u}{\partial z}. \quad (9)$$

3) approach a_3, no advective terms.

$$a_{h1} = a_{h2} = \frac{\partial u}{\partial t}. \quad (10)$$

Note that only the local acceleration is included in the standard Morison's equation (a_3). Models a_1 and a_2 can be regarded as *modified* Morison models. We have not included the surface intersection force from [31], or the $F^{\eta\prime}$ term from [14]. Additionally, viscous drag terms have been found to be negligible and are therefore not included. All of the simulations in the present work consider 2nd order wave kinematics and the loads are integrated up to the undisturbed 2nd order wave elevation.

In order to obtain the second order wave kinematics, the measured wave elevation signal is first linearized through a bandpass filter. The high-frequency cut-off of this filter is selected through an iterative procedure in order to best match the measured wave elevation spectrum. This iterative procedure is carried out for each calibrated wave signal. An example of the wave spectrum reconstruction is given in Fig. 5. As shown, we do not attempt to reconstruct the low-frequency components of the measured spectrum. The measured low-frequency components include both difference-frequency components, parasitic waves generated in the basin, and some resonant modes of the basin, while the reconstruction does not include the difference-frequency terms. A reasonable match for the high-frequency tail is obtained.

There are important limitations regarding the selected wave kinematic model and wave load model applied in the present work. For very steep regular waves, second order wave kinematics have been found to overestimate the measured velocity field [32]. Compared to the wave conditions in [32], the irregular waves studied here correspond to lower wave height to water depth ratio ($H/h \approx 0.3$) and shorter non-dimensional period ($T\sqrt{gh} \approx 7.4$). Still, some overestimation of wave kinematics may be expected.

4. Uncertainty assessment

4.1. Response metrics

In order to be able to assess the experimental uncertainty, well-defined response metrics, or quantities of interest, are needed. These response metrics have to be quantities which can be measured or computed directly from the measurements, and which can also be predicted numerically. For simplicity, scalar (rather than time series) quantities are desirable. For the present work, we define the following response metrics:

1) Bending moment transfer function, denoted response amplitude operators (bending moment RAOs) at $z = -28.5$ m for the first, second, and third harmonic of the primary wave frequency for wave periods 6-15 s.
2) 90th percentile 30-minute bending moment response at $z = -28.5$ m for long-crested waves with $H_s = 9$ m and $T_p = 12.3$ s (TMA spectrum [33]).

The first response metric can be computed from the long-crested regular waves, while the second is obtained from the realizations of irregular waves.

The bending moment RAO for the first harmonic component is defined as the amplitude of the bending moment at the primary wave frequency divided by the amplitude of the wave elevation at the primary wave frequency. Here, the amplitude is determined by first bandpass filtering the time signal of interest, then taking the average amplitude over a time range after the ramp in the wave amplitude, but before the return of reflected waves from the beach. The second and third harmonic response components are divided by the first order wave amplitude raised to the power of 2 or 3, respectively, in the chosen definition of the RAO for the second and third harmonic responses. The amplitude of the higher harmonic components is determined using bandpass-filtered time signals before reflections, in a similar manner to the first order RAO.

Although the 90th percentile 30-minute maximum bending moment is not typically a design parameter of interest (one might instead be interested in the 3-hour maximum bending moment), it is selected as a response metric for practical reasons. Each 3-hour realization can be divided into 6 30-minute periods. The 90th percentile 30-minute maximum is estimated by fitting a Gumbel distribution to the maxima from each of the 30-minute periods. The method-of-moments is used for the fitting process. The uncertainties induced by the fitting process are not examined here.

For the experiments, the uncertainty in these response metrics will depend on the uncertainty in the incoming waves, the model itself (i.e. geometry, stiffness, mass distribution), and the measured response (bending moment). The numerical simulations include uncertainty in the discretization, the wave input (in this case, in the filtering of the measured wave), and in the load model (in this case, the coefficients in the Morison model). Oberkampf et al. [34] present a framework for error and uncertainty analysis in modeling partial differential equations, considering epistemic and aleatory uncertainty, acknowledged errors, and unacknowledged errors in six phases of modeling and simulation. The present work does not attempt to quantify the uncertainty in the numerical analysis, but focuses on the experimental uncertainty.

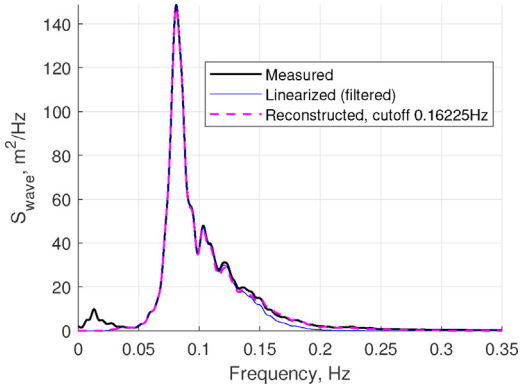

Fig. 5. Second order reconstruction of the measured wave elevation, $H_s = 9$ m and $T_p = 12.3$ s.

4.2. Experimental uncertainty

Experimental uncertainty is typically expressed in terms of random (aleatory or statistical) uncertainty and systematic (bias, systemic) uncertainty [35,36]. Random uncertainties are related to inherent random variations in a physical process. The level of random uncertainty can be assessed through repeated tests. Systematic uncertainties may create an unknown bias in the tests. Without additional information, there is no way to reduce these uncertainties, and their magnitude is typically estimated through expert opinion.

The random standard uncertainty of a response which is measured repeatedly is found from:

$$s_R = \frac{s_x}{\sqrt{N-1}} \quad (11)$$

where s_x is the standard deviation of the measured quantity over N

repeated tests. Repeated tests capture the random uncertainty in measurement and in the physical process simultaneously - the variation between different repeat tests does not give us information about the source of the variation.

The effect of a systematic uncertainty on the uncertainty of the response variable of interest must be obtained through uncertainty propagation. Where multivariable dependencies are involved, the uncertainty propagation may be carried out based on known relationships between the dependent variables and measured variables [37]. A linearization of a known functional relationship can be used to find a sensitivity index. Considering a result R which depends on L independent variables x_i, the sensitivity index θ_i is given by

$$\theta_i = \frac{\partial R}{\partial x_i}, \quad i = 1, 2, ...L, \tag{12}$$

and evaluated at either mean or nominal values of the result. A similar sensitivity index can be obtained by sequential perturbation [37]. The uncertainty in the result due to the systematic uncertainties is obtained by the square root of the sum of squares (RSS) of the contributions from all of the independent variables:

$$u_R = \pm\sqrt{\sum_{i=1}^{L}\left(\theta_i u_{\bar{x}_i}\right)^2} \tag{13}$$

where $u_{\bar{x}_i}$ is the best estimate of the uncertainty in the independent variable.

In order to combine the random and systematic uncertainties, the RSS is again used:

$$u_c = \sqrt{(u_R)^2 + (s_R)^2}. \tag{14}$$

The total uncertainty from Eq. (14) is shown in the results in the present work. It should be noted that one could also present the expanded uncertainty (equal to twice the total uncertainty for a 95% confidence interval) [36]. In the following subsections, we first present an assessment of the level of repeatability in the tests. Next, the estimated bias errors in the measurements of the model, waves, and responses are described. Then, a simplified model which enables the propagation of bias errors is presented. Finally, the total experimental uncertainty in selected response metrics is estimated using both the simplified model and through numerical simulations with model a_3 described in Section 3, and the contributions of different factors are compared.

4.2.1. Repeatability

Repetition tests - where an identical signal was sent to the wavemaker - are useful for assessing the repeatability of the results. Due to the time-consuming nature of such tests, there are few published examples of extensive repetition tests with a flexible model in a wave basin. Fig. 6 shows one of the largest response events for one realization of the sea state with $H_s = 9$ m, and $T_p = 12.3$ s, which was run in total 9 times with the model and 3 times without the model. The repeatability of this particular event is, however, not particularly impressive: the coefficient of variation (ratio of standard deviation to the mean) of the maximum bending moment is 0.18. The calibrated wave (measured at the model, shown in red) and the wave measured far from the model (but at the same x-location) have coefficients of variation of 0.07 and 0.08, respectively.

Despite the automation in the test procedures, the repeatability of the tests observed here is lower than typically seen in tests in the Ocean Basin. There are several factors which contribute to this relatively low repeatability. First, wave generation at relatively small depths (as in the present work) is very sensitive to the local water depth. The basin floor is moveable, and though it was fastened carefully at 16 locations, there are still local variations in the bottom and there is some possible deformation of the bottom. Second, there are non-deterministic processes associated with breaking waves. Although breaking waves were not the main focus of the present work, there were breaking waves present in most of the studied sea states. Finally, the level of damping in the system was extremely low. There are important memory effects in the response of a lightly damped flexible monopile (see [9]), and the system may continue to respond to events (including breaking wave events) long after the wave has passed, thus changing the system's interaction with subsequent waves.

Assessing the repeatability of the RAO is challenging for several reasons. First, the generation of regular waves in relatively shallow water can be challenging due to the previously mentioned depth variations and reflections, standing waves, and parasitic waves in the basin. The variation of the wave amplitude along the harp during calibration, shown in Fig. 7, exemplifies these challenges. There are notable differences in the amplitude of the first harmonic of the wave, especially for the longest waves. The wave amplitude at a given location along the harp deviates up to 18% compared to the mean amplitude, and the coefficient of variation ranges from 3 to 9% depending on the wave period. The second reason that it is difficult to assess the repeatability of the RAO is that few repetition tests were carried out.

Fig. 8 shows the computed RAO for all of the regular waves. For a linear system under linear wave loads, the RAO for different wave steepnesses would be equal. There is good agreement in the first harmonic RAO for longer waves, while for the shorter waves and the higher harmonics there are some nonlinear effects, leading to different RAO values for different wave steepnesses. These nonlinear effects may be related to the load mechanisms at the first order frequency, or to interactions between first and higher order wave load components. For example, the 2ω wave loads when $T = 8$ or 9 s, resulting in resonant responses, may change the first harmonic loads and responses due to hydroelasticity or other interactions. The repeated tests also showed

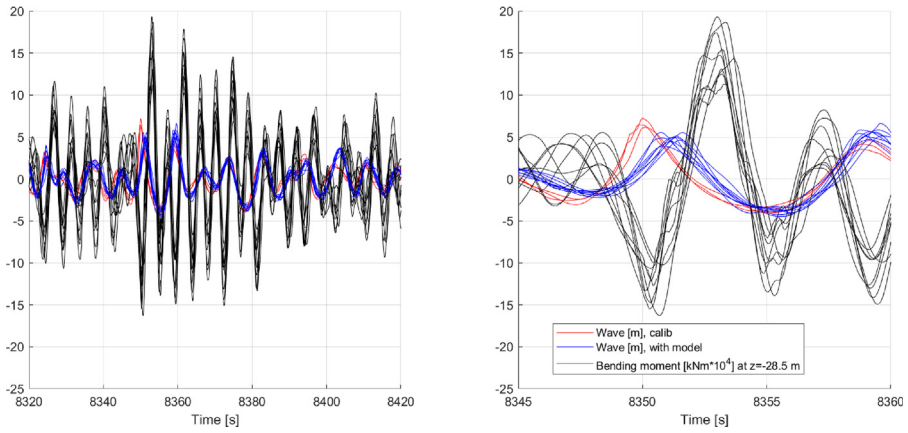

Fig. 6. Repeatability of a severe wave event, $H_s = 9$ m and $T_p = 12.3$ s. The wave with the model is measured 200 m from the model in the y-direction.

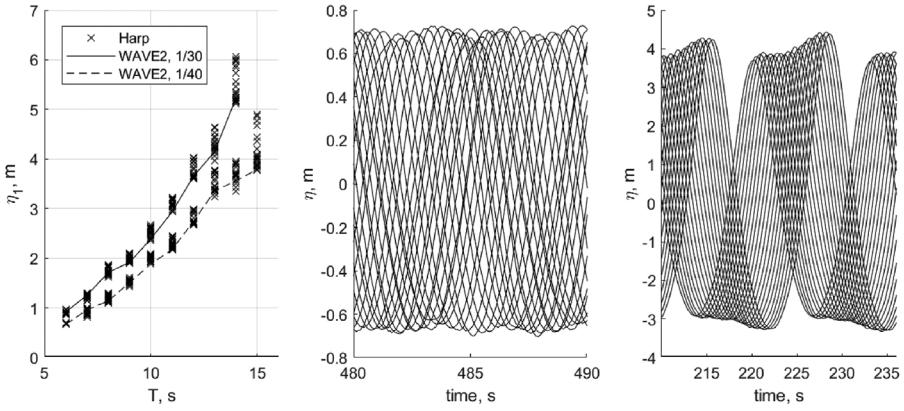

Fig. 7. Variations in regular wave amplitude along the wave harp. Left: amplitude of the first harmonic of the wave along the harp, where WAVE2 shows the value at the model location. Note that the indicated steepnesses 1/30 and 1/40 are approximate. Middle: time series of wave elevation along the harp (T = 6 s, lower steepness). Right: time series of wave elevation along the harp (T = 13 s, lower steepness).

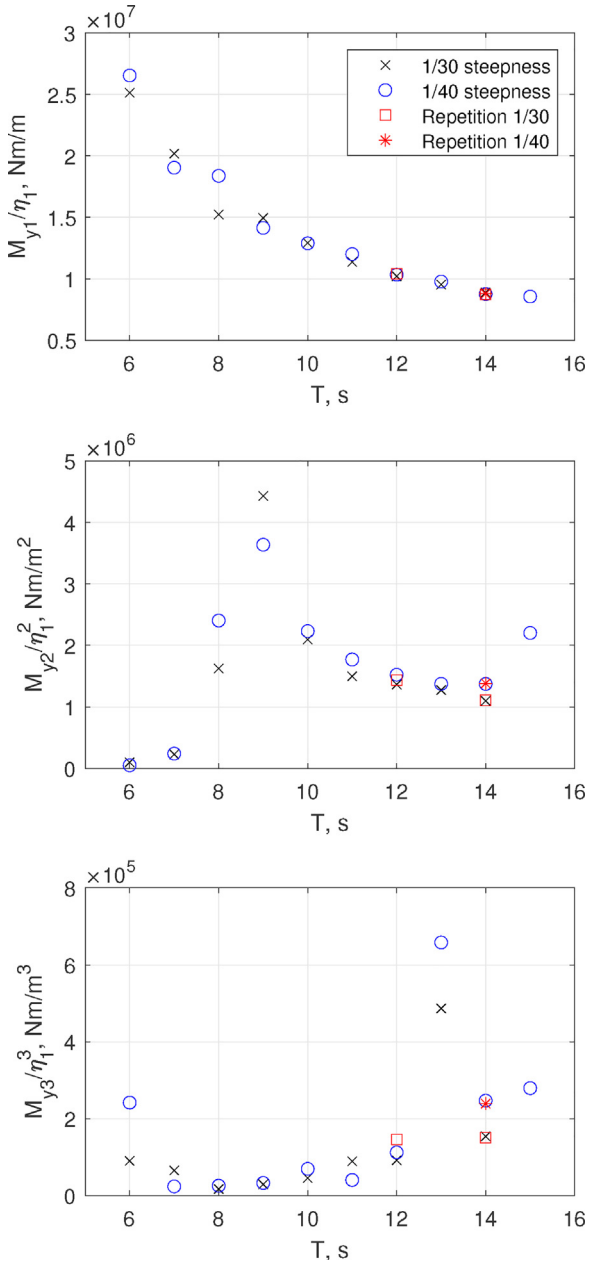

Fig. 8. Experimental bending moment (at $z = -28.5$ m) RAO results, highlighting the repeatability and the differences in results for different wave steepness.

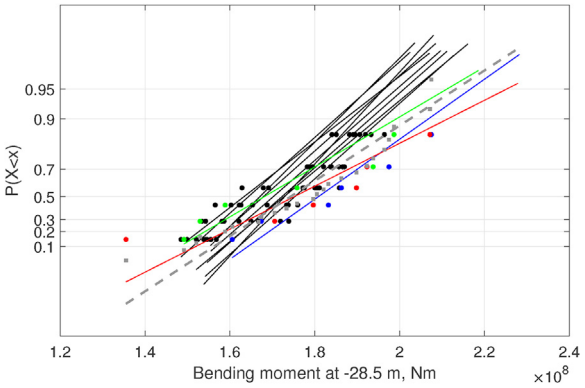

Fig. 9. Gumbel fitting of the 90th percentile 30-minute maximum bending moment (P = 0.9 in the figure) for H_s = 9 m and T_p = 12.3 s, from experimental data. Dots show 6 maxima from each 3-hour experimental realization, while lines show fitted Gumbel distributions based on those maxima. Black lines/points are repetition tests of the same seed, while colors show different seeds. The dashed gray line shows the results considering 24 maxima (using the first of the repetition tests and three additional seeds).

Table 5
Estimated bias errors. All values given in full scale.

Parameter	Bias error
Measured wave elevation	± 3%
Water depth	± 0.4 m
Mass distribution	± 10% locally
Inner core dimensions	± 4 mm
Outer shell dimensions	± 6 cm
Strain	± 0.5%
Acceleration	orientation ± 2.5°, location 0.12 m

good agreement (within 2%) for the first harmonic.

The RAO for the second harmonic of the response shows significant amplification when the wave period was 8-9 s, which is close to twice the natural period of the monopile. The discrepancies between the results for the different wave steepnesses were large, but the repeatability of each condition was within 5%. For the third harmonic, the peak occurred for periods near 3 times the structural natural period. The repeatability at 12 s is seen to be quite poor, which may be related to the dynamic amplification near this period giving great sensitivity. It should also be noted that the higher order responses tend to be less stable than the first order response, so the results may be sensitive to the selected time period for analysis.

Fig. 9 illustrates the variation in the 30-minute 90th percentile bending moment near the seabed for irregular waves with H_s = 9 m and T_p = 12.3 s. The variation among repetitions of the same seed give similar results for the 90th percentile bending moment: the coefficient of

Table 6
Independent input variables for semi-analytical analysis. (1) The variation in stiffness is found based on the possible error in inner core dimensions at the most sensitive point.

Input variable	Symbol	Comments
Mass distribution	m	Affects modal parameters. Uniform relative variation 10%.
Stiffness distribution	EI	Affects modal parameters. Uniform relative variation 4%[(1)].
Modal damping	b_i or ζ	Varied for all five modes simultaneously 20%.
Outer diameter	D	Only affects wave loads. 6 cm.
Water depth	h	Affects modal parameters and wave loads. 0.4 m
Regular wave period	$2\pi/\omega$	Affects wave loads. 0.05 s.
Irregular wave significant wave height	H_s	Maintain spectral shape. 3%.
Irregular wave peak period	T_p	Maintain spectral shape. 0.05 s.

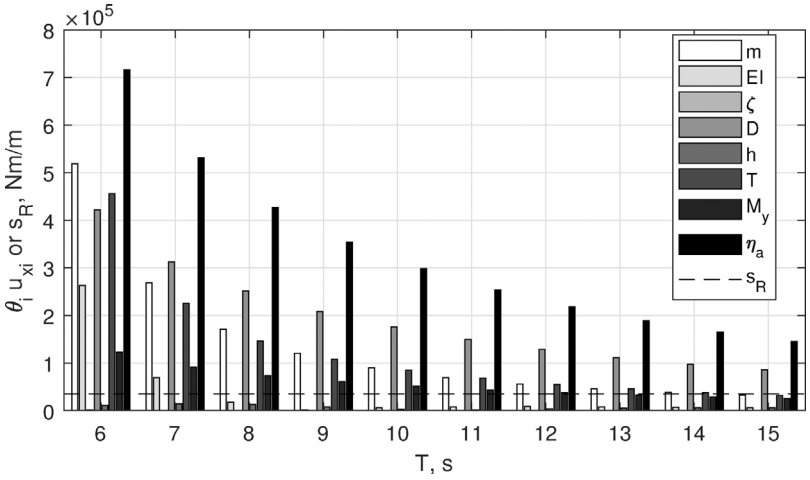

Fig. 10. Contributions to the experimental uncertainty for the first order bending moment RAO, using the simplified model. Contributions u_R (i.e. terms inside the summation of Eq. (13)) are shown in the columns for each wave period, while the random uncertainty s_R (Eq. (11)) is shown as a dashed line (assumed to be equal for all wave periods).

variation for those 9 estimates is 2%. Comparing the mean of these 9 estimates with the predictions from three additional seeds gives a coefficient of variation of 4.7%. The statistical results for the irregular waves are seen to be more repeatable and more stable than the individual events (such as the one shown in Fig. 6).

4.2.2. Estimated bias errors

The bias errors in the wave elevation measurements, physical model properties, and acceleration and bending moment measurements are summarized in Table 5.

The waves are measured using resistive-type wave gauges, which are calibrated by moving the waves gauges up and down in still water. Bias errors in the wave measurements can arise if the gauge is not completely vertical, if the distance over which the gauges are moved during calibration is incorrectly measured, due to temperature effects, or changing water levels during calibration. The temperature variations during the model tests were ± 0.07 °C, and the wave gauges have a sensitivity of 2%/deg C. Temperature effects had a relatively small contribution to the bias error for the wave gauges.

The total mass and the center of mass were measured prior to dry-testing the model. The local mass distribution is, however, estimated, and a large uncertainty in the mass distribution can be seen to exist due to the extensive instrumentation in the model.

Strain (ϵ) measurements are used to estimate the bending moment in the structure. The functional relationship between the measured strain and the bending moment is based on Hooke's law:

$$\sigma = \epsilon E = \mathrm{E}\, y w_{zz} = \mathrm{M}y/I \tag{15}$$

where σ is stress, E is Young's modulus, y is the radial location of the strain measurement, I is the area moment of inertia of the cross-section, and w_{xx} is the local curvature. The bending moment is then seen to be linearly related to the measured strain. Calibration of the strain gauges is carried out by applying a known moment (via a hanging weight attached through a pulley at a given height), such that for our purposes, the sensitivity of the moment measurement to error in the strain measurement is captured by the linear calibration factor. We estimated the bias error by considering ± 2 mm model scale error in height and ± 5 degrees error in orientation of the load applied for calibration. Based on the manufacturer data, the temperature error in the moment is 0.03% per degree C: considering temperature variations ± 0.07 °C, the temperature contribution to the bias is negligible compared to the previously described contributions.

The bias error in the acceleration measurements is reported, but is not used in the rest of the analysis, since the focus is on the bending moment measurements.

4.2.3. Simplified semi-analytical uncertainty propagation

In order to carry out propagation of bias errors using analytically obtained sensitivities, a simplified model is needed. Furthermore, in general, it is preferable to use different numerical models for the propagation of uncertainties compared to the numerical model one wishes to investigate. Here, we first consider a simplified model for the response of the monopile. This simplified model is used to propagate bias errors in the properties of the physical model and in the incoming waves to the bending moment response.

For the present system, a linearized model is obtained by combining a 5-mode structural response model with linear wave loads considering only the inertia term from Morison's equation. The number of modes was selected based on a convergence study using the simple model.

The structural response model takes the form of the decoupled ordinary differential equations in Eq. (16), where $\bar{m}_i$ is the modal mass, $\bar{b}_i$ is the modal damping, $\bar{k}_i$ is the modal stiffness, $\bar{F}_i$ is the modal force, and y_i is the modal response.

$$\bar{m}_i \ddot{y}_i + \bar{b}_i \dot{y}_i + \bar{k}_i y_i = \bar{F}_i, \quad i = 1, 2, 3, 4, 5 \tag{16}$$

For a uniform beam, analytical expressions for $\bar{m}_i$ and $\bar{k}_i$ are easily derived. Due to the complexity of the present system (with varying

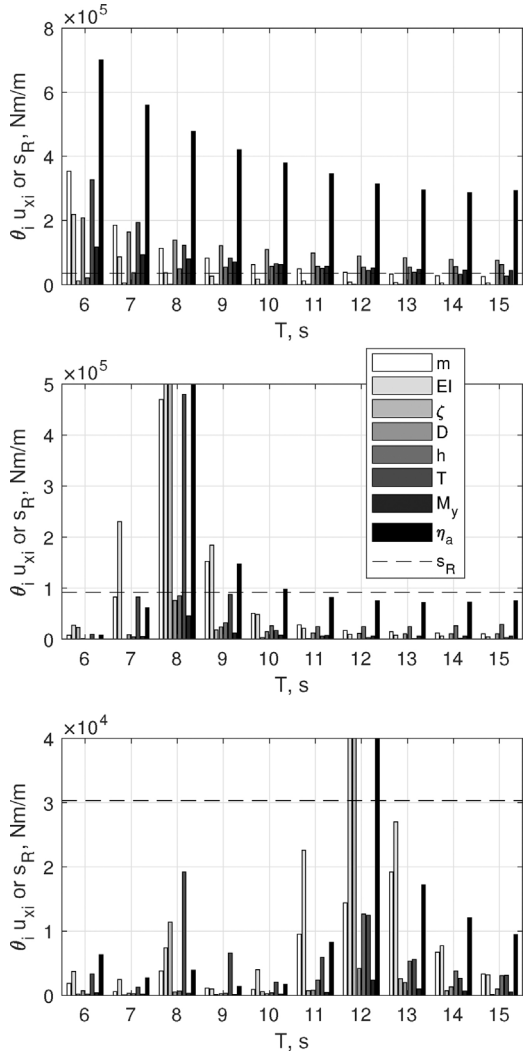

Fig. 11. Contributions to the experimental uncertainty for the bending moment RAO, computed using SIMA. Top: first harmonic, middle: second harmonic, bottom: third harmonic. Contributions u_R (i.e. terms inside the summation of Eq. (13)) are shown in the columns for each wave period, while the random uncertainty s_R (Eq. (11)) is shown as a dashed line (assumed to be equal for all wave periods).

stiffness and density), it is more convenient to apply a finite element model rather than developing the analytical expressions. In the present work, the same Euler beam model from RIFLEX is used in order to obtain the mode shapes φ_i. Since the software does not easily output the modal mass and stiffness, we can apply Eqs. (17) and (18) together with the known mass distribution (including added mass) and stiffness distribution to obtain these parameters. The undamped natural frequencies obtained from the estimated modal mass and stiffness were found to be within 5% of those from the eigenvalue analysis. The discrepancy is probably due to the simplifying assumptions which lead to Eqs. (17) and (18), and the sensitivity of the derivatives of the discretized mode shapes. In order to maintain the same natural frequencies, the modal mass was modified to give matching results.

The vertical integration in Eqs. (17) and (18) is over the full length of the monopile and tower. There are contributions to the modal mass from the distributed mass per length $m(z)$ (including added mass) as well as point masses (M_j) and inertias (I_j). The modal stiffness is governed by the local bending stiffness, consisting of the Young's modulus E and area moment of inertia I.

$$\bar{m}_i = \int_{z_{low}}^{z_{top}} m(z)(\varphi_i(z))^2 \mathrm{dz} + \sum M_j(\varphi_i(z_j))^2 + \sum I_j(\varphi_{i,z}(z_j))^2 \tag{17}$$

$$\bar{k}_i = \int_{z_{low}}^{z_{top}} \mathrm{EI}(z)(\varphi_{i,zz}(z))^2 \mathrm{dz} \tag{18}$$

For simplicity, the modal damping is chosen to give the same damping ratio in all five modes. Based on the decay tests, $\zeta = 0.5\%$ critical damping is chosen.

$$\bar{b}_i = 2\bar{m}_i\omega_{0,i}\zeta = 2\zeta\sqrt{(\bar{k}_i\bar{m}_i)} \tag{19}$$

The structural model with n modes ($n = 5$ here) can be used to obtain the total deflection at any point along the structure:

$$w_{\mathrm{struct}}(z, t) = \sum_{i=1}^{n} y_i(t)\varphi_i(z). \tag{20}$$

The local accelerations ($\frac{\partial^2 w}{\partial t^2}$) and curvatures ($\frac{\partial^2 w}{\partial z^2}$) can then be used to evaluate the sensitivity of measured quantities to uncertainties in the independent inputs.

The external loads in this simplified model are based on the inertia term from Morison's equation:

$$\mathrm{dF} = \rho(C_a + 1)\pi\frac{D^2}{4}\mathrm{a\ dz} \tag{21}$$

where ρ is the water density, C_a is an inertia coefficient, D is the wetted diameter, and a is the wave particle acceleration. For the simple uncertainty propagation model, linear Airy wave theory is used to find a. The viscous drag forces are neglected because they are small and in order to maintain a linear model. In the modal response model, the Morison inertia load takes the form:

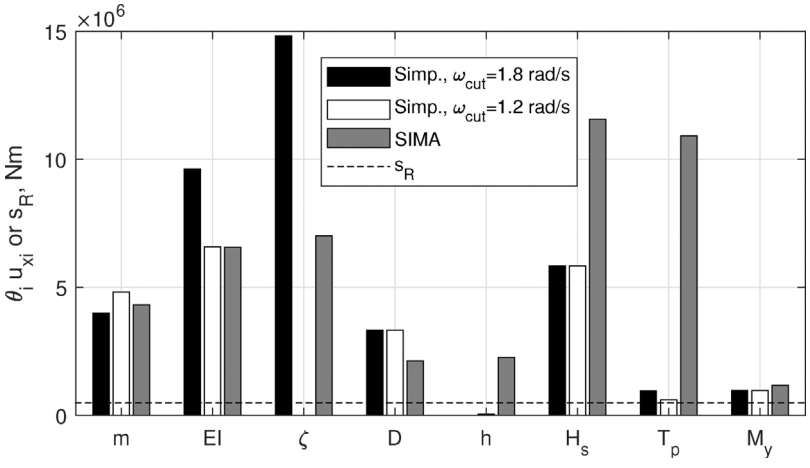

Fig. 12. Contributions to the experimental uncertainty in the 90th percentile 30-minute bending moment response at $z = -28.5$ m for long-crested waves with $H_s = 9$ m and $T_p = 12.3$ s, depending on wave spectrum cut-off frequency in the simplified uncertainty propagation model. Contributions to u_R are shown as columns, while s_R is shown as a dashed line.

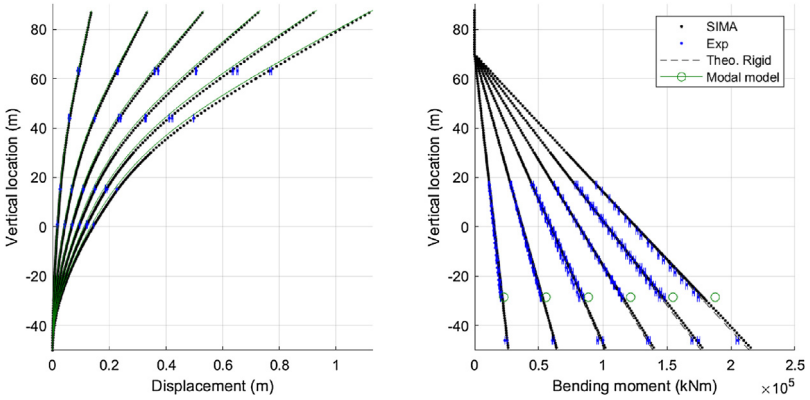

Fig. 13. Selected pullout test results.

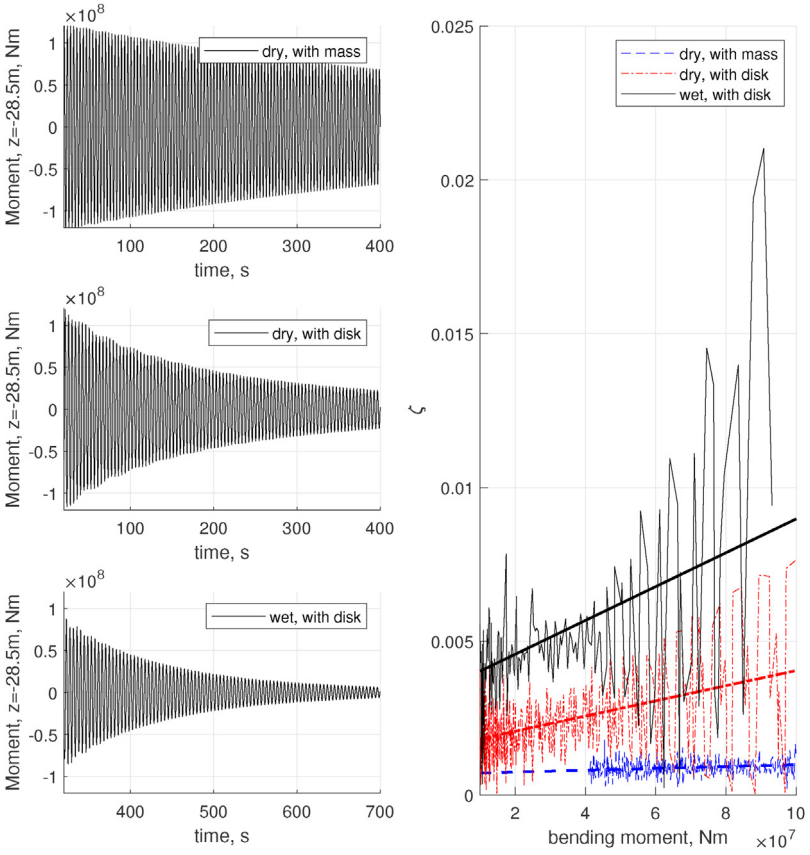

Fig. 14. Decay test results, model hit from the top. Left: mudline bending moment time series. Right: damping ratio calculated by logarithmic decrement.

Table 7
Eigenfrequencies of the experimental model, numerical model of the experiments, and the reference prototype. Differences are computed between the experimental model and the numerical model of the experiment.

Configuration	Mode	Exp. (Hz)	Num. (Hz)	Diff (%)	Prototype (Hz)
Dry, mass at the top	1	0.26	0.27	2.7	N/A
	2	1.09	1.03	5.2	N/A
	3	4.06	3.85	5.0	N/A
Dry, aerodynamic disk	1	0.24	0.24	0.9	N/A
	2	1.00	0.91	8.9	N/A
	3	2.69	2.27	15.8	N/A
Wet, aerodynamic disk	1	0.22	0.24	8.2	0.26
	2	0.85	0.85	2.9	1.07
	3	2.40	2.11	11.8	3.22

$$\bar{F}_i = \int_{-h}^{0} \varphi_i(z)\rho(C_a + 1)\pi\frac{D^2}{4}\mathrm{a}\,\mathrm{dz}, \tag{22}$$

with a for regular waves with amplitude η_a and frequency $\omega = 2\pi/T$ in water depth h given by:

$$a = \omega^2\eta_a\frac{\cosh(k(z+h))}{\sinh(\mathrm{kh})}\cos(\omega t). \tag{23}$$

According to this simple semi-analytical model, the first response metric, the first harmonic bending moment RAO at $z_j = -28.5$ m is given by Eq. (24). Eq. (24) consists of the bending moment response (from superposition of the modal responses to the distributed load in Eq. (21)) divided by the incoming wave amplitude. The wave amplitude η_a in the denominator is cancelled by the same term which appears in the acceleration (Eq. (23)). The higher wave harmonic responses are not captured by this model due to the simplifications in the excitation

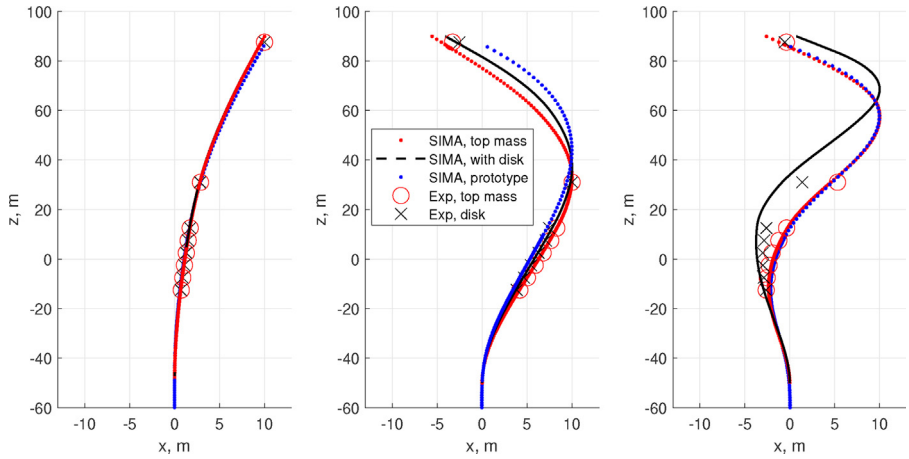

Fig. 15. Numerically and experimentally obtained dry mode shapes for modes 1-3. (Prototype modes are for wetted monopile).

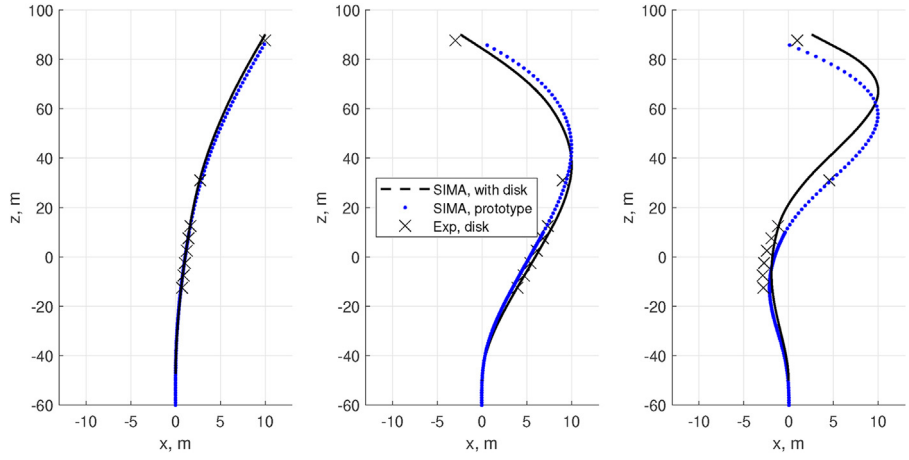

Fig. 16. Numerically and experimentally obtained wet mode shapes for modes 1-3.

force.

$$|H(\omega)| = \frac{|M|_{z_j}|}{|\eta_a|} = \sum_{i=1}^{n} \mathrm{EI}(z_j)\varphi_{i,zz}(z_j)\frac{\int_{-h}^{0}(C_a+1)\frac{\pi D^2}{4}\rho\omega^2\frac{\cosh(k(z+h))}{\sinh(\mathrm{kh})}\varphi_i(z)\mathrm{d}z}{\bar{k}_i\sqrt{((1-\beta_i^2)^2+(2\zeta_i\beta_i)^2)}} \quad (24)$$

In Eq. (24), β_i is the frequency ratio for each mode:

$$\beta_i = \frac{\omega}{\omega_i} = \frac{\omega\sqrt{\bar{m}_i}}{\sqrt{\bar{k}_i}}. \quad (25)$$

Using the RAO in Eq. (24), the response spectrum in linear irregular waves for this simple model is given by Eq. (26), where S_M is the response and S_w is the wave spectrum (see e.g. [38]).

$$S_M(\omega) = S_w(\omega)|H(\omega)|^2 \quad (26)$$

For the present experiments, a TMA wave spectrum [33] is applied. The TMA wave spectrum modifies the JONSWAP spectrum (S_J) for finite water depth. The JONSWAP spectrum is itself a modification of the Pierson-Moskowitz spectrum (S_{PM}). Following the notation from DNV [27]:

$$S_{\mathrm{PM}}(\omega) = \frac{5}{16}H_s^2\omega_p^4\exp\left(-\frac{5}{4}\left(\frac{\omega}{\omega_p}\right)^{-4}\right), \quad (27)$$

$$S_J(\omega) = A_\gamma S_{\mathrm{PM}}(\omega)\gamma^{\exp\left(-0.5\left(\frac{\omega-\omega_p}{\sigma_J\omega_p}\right)^2\right)}, \quad (28)$$

where $\omega_p = 2\pi/T_p$ is the peak spectral frequency, γ is the spectral peak shape factor, σ_J is a spectral width parameter, and A_γ is a normalizing factor. The TMA spectrum is written as

$$S_w(\omega) = S_J(\omega)\phi_{\mathrm{TMA}}(\omega). \quad (29)$$

For intermediate water depth, following [33], the depth function is computed in terms of the wave number k as in Eq. (30) (note that this differs from the expression in [27]).

$$\phi_{\mathrm{TMA}} = \frac{\sinh^2(\mathrm{kh})}{\cosh^2(\mathrm{kh}) + \mathrm{kh}\coth\mathrm{kh}}, \quad (30)$$

with $\omega^2 = gk\tanh(kh)$.

Assuming a Gaussian wave elevation, following [38], the response which with probability p will not be exceeded over time T can be estimated as

$$\xi_p(T) = \sigma_x\sqrt{2\ln\left(\frac{\nu_x^+(0)T}{\ln(1/p)}\right)} \quad (31)$$

In Eq. (31), the standard deviation σ_x can be found from the zeroth spectral moment (Eq. (32)), while the zero upcrossing rate $\nu_x^+(0)$ can be estimated based on the zeroth and second spectral moments. For the response metric defined previously, $T = 30$ min.

$$\sigma_x^2 = \int_0^\infty S_M\,d\omega \quad (32)$$

$$\nu_x^+(0) = \frac{1}{2\pi}\frac{\sigma_x}{\sigma_{\dot{x}}} \quad (33)$$

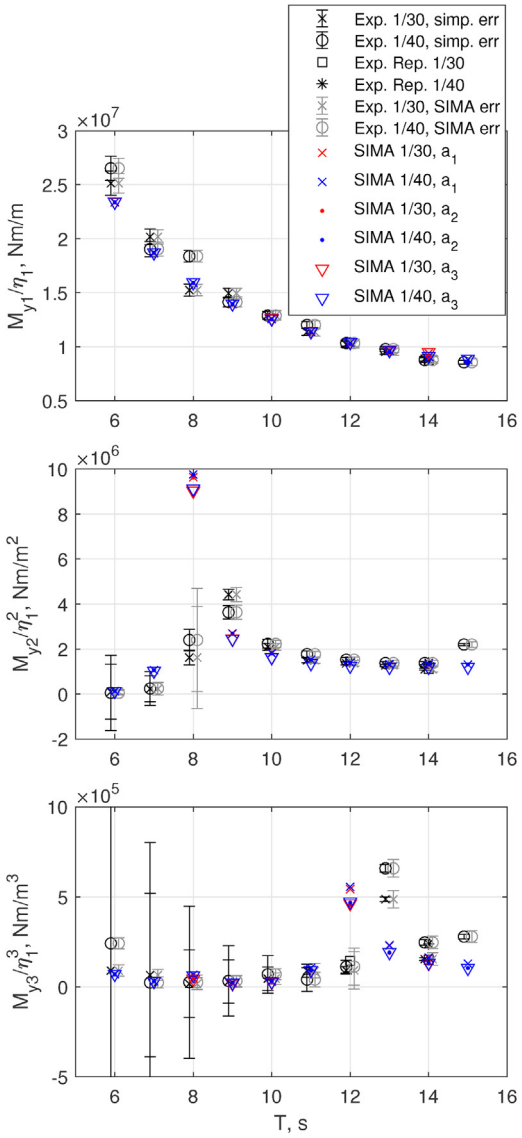

Fig. 17. Comparison of numerical and experimental mudline bending moment RAO from the regular wave tests. Experimental results are slightly shifted along the x-axis for readability. Error bars indicate total uncertainty as in Eq. (14). The amplitude of the total uncertainty for the lowest frequency for the 3rd harmonic using the simplified uncertainty analysis is approximately 2.5×10^6 Nm/m^3.

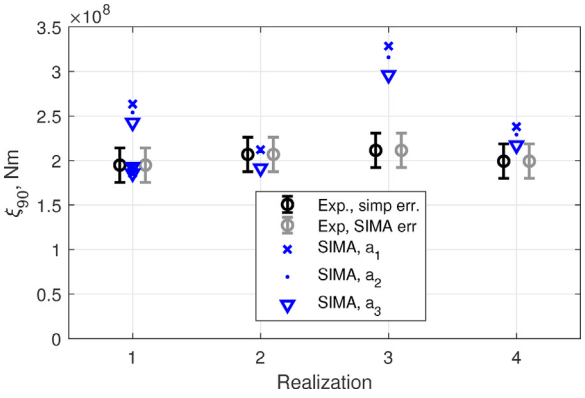

Fig. 19. Comparison of numerical and experimental 90th percentile 30-minute bending moment response at $z = -28.5$ m for long-crested waves with $H_s = 9$ m and $T_p = 12.3$ s. Experimental results are shifted along the x-axis to increase readability.

$$\sigma_{\dot{x}}^2 = \int_0^\infty \omega^2 S_M \, d\omega \tag{34}$$

Table 6 summarizes the variables which can be considered as inputs to this simple model, as well as their interpretation with respect to the measurement bias errors given in Table 5. The sensitivity to each of these inputs can be computed by analytical derivation, combined with discrete derivation where needed. Any variables which affect the modal parameters, for example, require re-calculation of the modal parameters in addition to analytical derivations. For distributed parameters (mass and stiffness), a uniform relative variation is assumed for simplicity. This may, however, give a significant overestimation of the total uncertainty.

The height (or amplitude) of regular waves does not affect the RAO in this simple linear model, so this variable is not included in Table 6. The regular wave height is instead considered as a part of the measurement model.

To compute the total bias error in the measured response, we combine the effects of the inputs in Table 6 with the effects of the estimated bias errors in the wave elevation and bending moment measurements.

4.2.4. *Total experimental uncertainty*

Using the simplified model presented in Section 4.2.3, the experimental uncertainty in the RAO for the first harmonic bending moment is shown in Fig. 10. For each wave period, the contributions to the bias error are shown by columns, while the random error (based on the few available repetitions, taken to be constant across all periods) is shown as a dashed line. The predicted baseline RAO for the simplified model

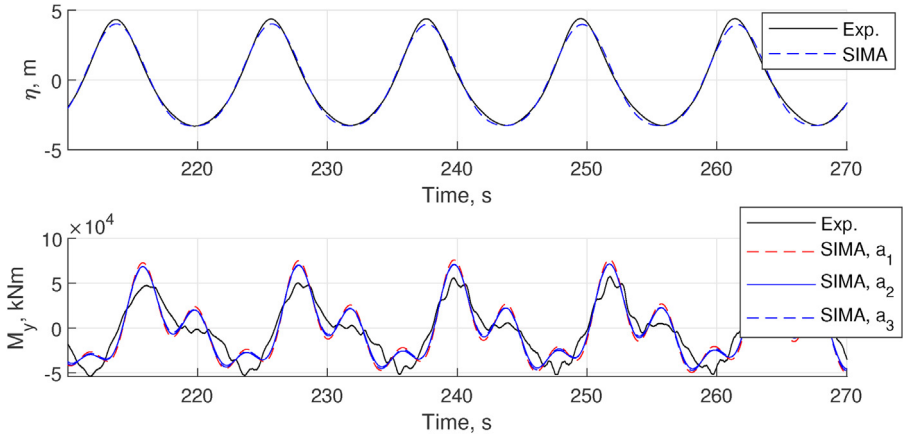

Fig. 18. Numerical and experimental time series of wave elevation (without model present) and mudline bending moment, $H = 7.5$ m, $T = 12$ s.

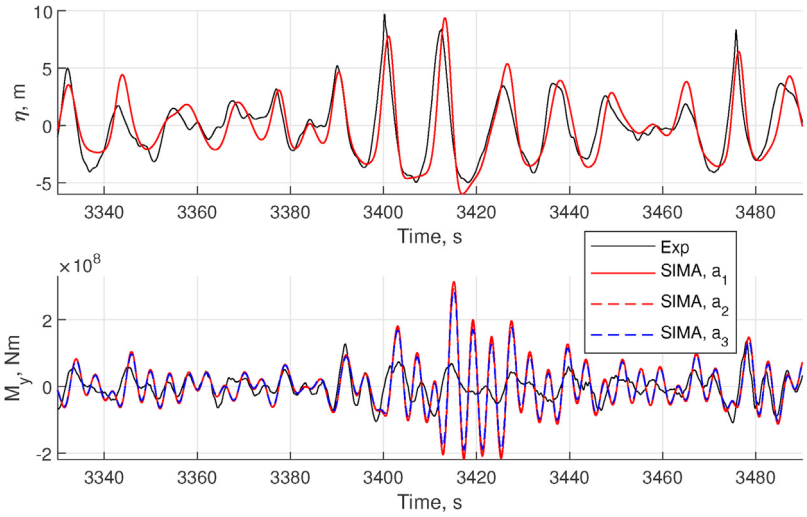

Fig. 20. Comparison of time series of wave elevation (next to the model, with model present) and mudline bending moment, H_s = 9 m and T_p = 12.3 s, showing extreme overprediction in realization 3.

was in good agreement with the experimental results, and the propagated uncertainty could be computed directly. As shown, the bias errors are generally larger than the random error. The most important components of the bias error are the wave elevation, mass, and diameter. The bias errors generally decrease for longer wave periods, and the importance of the mass distribution becomes smaller for longer waves. This is as expected, since the monopile response becomes increasingly stiffness-dominated for long wave periods.

The total uncertainty for the regular wave results was also assessed using the SIMA model. As far as possible, time domain simulations were carried out considering the same variables as in Table 6. For the damping, the stiffness-proportional structural damping was increased (or decreased) by 20%. The wave elevation and period were modified by directly modifying the input time series (by multiplicative factors). The uncertainty in the mudline bending moment RAO for the first three harmonics of the response is shown in Fig. 11. As shown, the first order results are similar to those from the simplified model (Fig. 10). For the second and third harmonics, large uncertainties can be seen in the wave periods which produce resonant responses. This can also be seen in the random error: the third harmonic random error is relatively large due to the fact that the repeated tests were carried out for a period of 12 s.

The contributions to the uncertainty for the 90th percentile bending moment are shown in a similar manner in Fig. 12 for two different cut-off values for the irregular wave spectrum which is used in the simplified uncertainty propagation model, and for the SIMA model (only evaluated for H_s 9 m and T_p 12.3 s). The reason for using two different values for the cut-off frequency in the simple model is that the cut-off for linear waves ($\omega_{\text{cut}} = \sqrt{2g/H_s}$) suggested by Stansberg et al. [39] falls almost exactly at the first natural frequency of the structure (without considering errors in mass or stiffness). Since the parameter variations corresponding to bias errors induce changes in the natural frequency, it was judged to be more representative to allow the linear wave components to either excite the first bending mode of the structure for all variations, or to cut off the spectrum well below the natural frequency such that no linear waves could excite the natural frequency. Using the simplified model, the estimated 90th percentile bending moment was overpredicted when the cut-off was set high (ω_{cut} = 1.8 rad/s, representing unrealistic linear wave excitation of the first natural frequency) and underpredicted when the cut-off was set low (ω_{cut} = 1.2 rad/s, representing no excitation of the first natural frequency). The computed bias errors were therefore in each case scaled by the same factor needed to make the estimated 90th percentile bending moment from the simple model match the first repetition of the first seed of the experimental results.

As shown in Fig. 12, the selection of the cut-off frequency for the spectrum in the simple model affects the importance of the mass, stiffness, and damping terms, while the uncertainty due to diameter, water depth, significant wave height, peak period, and moment measurement is not dependent on the cut-off. This is as expected: without the high-frequency components of the spectrum, the response is stiffness-dominated such that the structural damping effects are negligible and inertia effects are relatively small. In the comparisons between the experimental and numerical results, the experimental uncertainty is shown according to ω_{cut} = 1.8 rad/s as this yields a larger uncertainty. As with the regular wave results, the uncertainty due to bias errors is large compared to the uncertainty due to random errors, and the mass, diameter, and wave elevation (through H_s) are important contributors. Compared to the first order RAO, the 90th percentile bending moment is more sensitive to the stiffness and damping: this is as expected, since the higher frequency responses become more important. The contributions to the experimental uncertainty estimated by the simplified and SIMA models are similar except that the SIMA model suggests larger importance of H_s and T_p for the bias errors. The inclusion of higher order wave loads in the SIMA model may explain this difference.

5. Experimental and numerical results

5.1. Pullout tests

Prior to installing the model in the basin, pullout tests were carried out on land in order to document the model's stiffness and check the consistency of the moment and shear force measurements. These tests were carried out by attaching a string to the model at a given height and statically loading the string (through a pulley) with known weights. The loads were incrementally increased and then decreased, such that all load levels were measured twice except for the highest load.

The displacement of the model was measured at various locations using potentiometric displacement sensors. These sensors are presumed accurate to 0.01 mm (model scale), but the alignment of the sensor and the applied load is more difficult to control. Considering a possible error of ± 5 degrees, error bars indicating ± 0.4% of the displacement are indicated in Fig. 13, which shows the experimental and numerical results for one pullout test.

As shown in Fig. 13, the measured displacements and bending moments agree well with the measured values. Larger deviations (not shown) could be seen for the shear force.

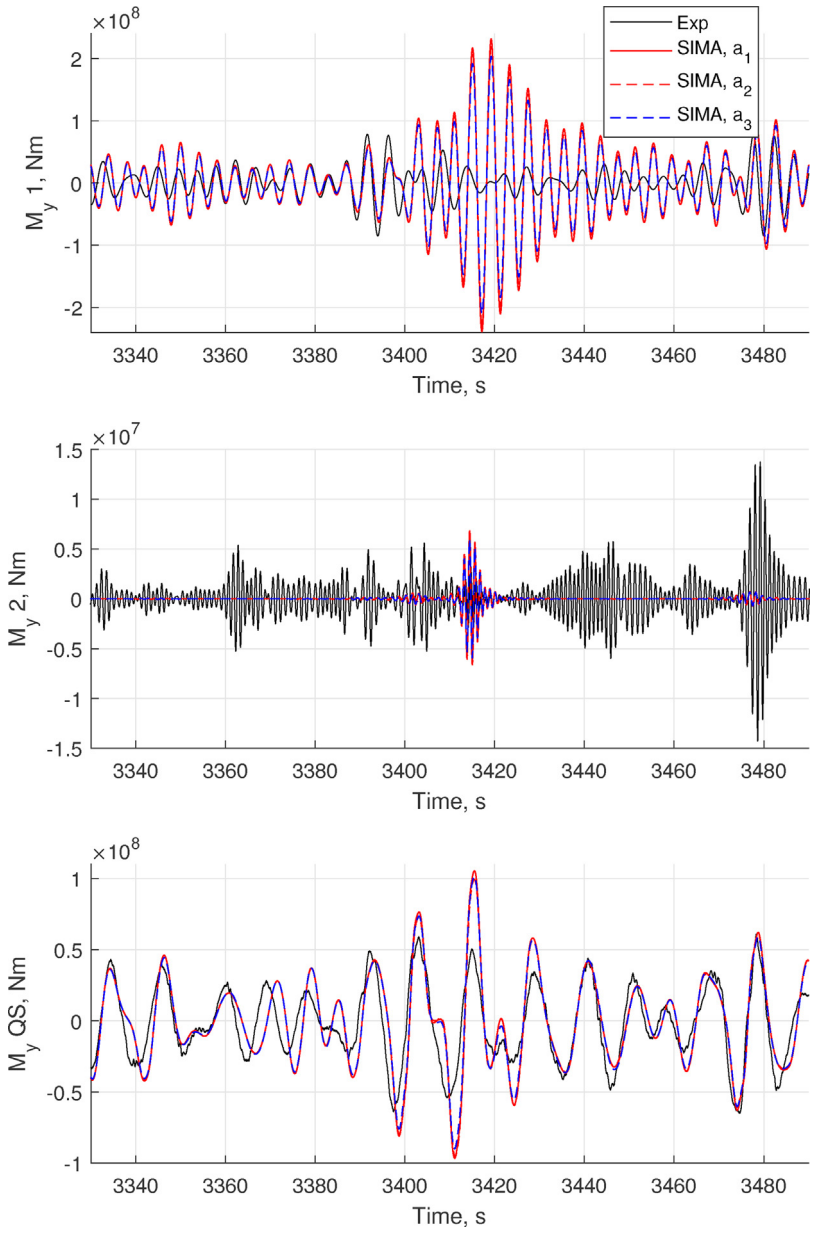

Fig. 21. Comparison of time series of mudline bending moment, bandpass filtered about 1st eigenfrequency (top), 2nd eigenfrequency (middle), and remainder (bottom). $H_s = 9$ m and $T_p = 12.3$ s, showing extreme overprediction in realization 3.

5.2. Decay tests

Decay tests were carried out to identify the eigenfrequencies and eigenmodes, and to quantify the different damping contributions. The tests were carried out in both dry and wet configurations, and the dry tests were carried out in two configurations: first with a simple mass at the top, then with the aerodynamic drag disk which was used in the tests with waves. During the decay tests, the model was either pulled and released, or simply hit, at different vertical locations.

The time series of the mudline bending moment and the calculated damping ratio for the first global bending mode (excited by hitting the top of the tower) are shown in Fig. 14. As shown, the dry test with top mass (no aerodynamic drag disk) shows primarily linear damping. This damping is considered as structural damping and modelled through stiffness-proportional Rayleigh damping in the numerical model. The presence of the aerodynamic drag disk increases both the linear and the quadratic damping. Comparing the two tests with the drag disk present, the decay test in water shows additional linear damping compared to the dry test. This damping is a combination of hydrodynamic radiation damping and hydrodynamic linear damping due to attached boundary-layer flow [40]. An earlier study with a pitching monopile [9] estimated the radiation damping to be on the order of 1% of critical damping. For the fully flexible monopile, the velocity of the wetted section of the monopile is much lower than that of the pitching monopile. As a result, both the radiation damping and the linear damping due to attached boundary-layer flow are significantly smaller. Simplified estimates assuming a linear deformation of the monopile under sea level suggest that the radiation damping contributes 0.16% of critical damping and attached boundary-layer flow contributions 0.03% of critical damping. This agrees with the observed increase in linear damping for the wet decay test compared to the dry test. The damping in the model tests is quite low compared to what might be expected for the prototype (1.7-2.8%) [41–43].

The obtained eigenfrequencies of the numerical and experimental models are summarized in Table 7. For reference, the corresponding eigenfrequencies of the 5 MW basis design, after which the

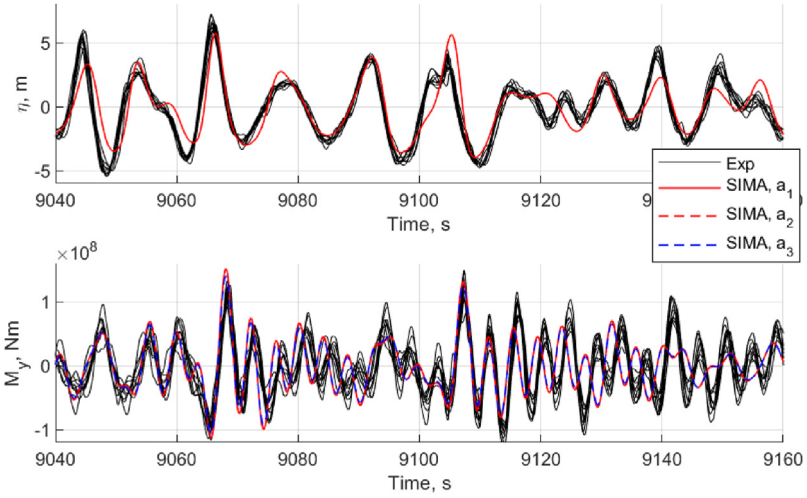

Fig. 22. Comparison of time series of wave elevation (next to the model, with model present) and mudline bending moment, $H_s = 9$ m and $T_p = 12.3$ s, showing good match for maxima. Repetition tests are included in the experimental results.

experimental model was designed, are also given. For the prototype, additional blade-related modes are present, but the selected frequencies correspond to the first three monopile/tower bending modes. The dry mode shapes are shown in Fig. 15. In the numerical model, when changing from the mass to the disk, the center of gravity of the mass is moved higher in addition to adding the inertia of the disk. This modification was made in order to capture the change in the first natural frequency.

As shown, the first mode shape does not depend strongly on how the RNA is modelled, while the second and third modes show greater variation. For the dry tests, the frequencies from the simulation model are within 6% of the measured values for the first two modes. The third mode is in good agreement for the model with just mass at the top, but the agreement is worse for the model with the disk. Qualitatively, the first and second mode shapes appear similar for the simulation and experimental models, but the accuracy of such a comparison is somewhat limited by the number of accelerometers along the model.

The wet mode shapes are shown in Fig. 16, while the frequencies are given in Table 7. Compared to the dry simulation model, added mass is included in the wet simulation model. The simulation model does not show as large of a change in the first modal frequency when moving from the dry to wet model. There are several possible reasons for the discrepancy: there may be some entrapped water within the monopile which is not captured by the numerical model, and the stiffness of the attachment in the basin may be softer than the dry set-up. The second of these two possibilities is judged to be most likely: an assumption that the model was completely hollow and became filled with water would have negligible impact on the natural frequency, while allowing the soil spring to be 20% softer could explain the observed difference.

The damping in the numerical model is implemented based on the experimental results: Rayleigh stiffness-proportional damping is used to match the linear damping contributions, while quadratic drag coefficients on the drag disk were used to match the quadratic damping contributions.

5.3. Regular wave tests

Fig. 17 compares the mudline bending moment RAO from the experiments and the numerical simulations. Error bars for the first order RAO indicate the total uncertainty as in Eq. (14), computed either using the simplified model or the SIMA model. This total uncertainty could further be increased to account for the expanded uncertainty [36], however this is not included in the present work. For the second and third order RAO, in the simplified uncertainty analysis, the total uncertainty from the first order RAO is divided by the first order wave amplitude (once or twice, respectively), in the same way that the second and third harmonic RAOs are computed. In the SIMA uncertainty analysis, the bias error in the second and third harmonic RAOs is estimated directly from the simulations.

The simulations in SIMA capture the main trends in the results, but do not match the experimental results within the estimated uncertainty bands for all frequencies. For the first order RAO, there is no difference in the numerical results between the different wave steepnesses. The experimental RAO shows some discrepancies in the first order RAO, especially for the 8 s wave. The 8 s wave corresponds approximately to twice the natural period of the first bending mode of the monopile, and there may be interactions among different frequencies in the load and response. The numerical simulations are also seen to give poorer agreement for the first order RAO for shorter wave periods. This agreement might be improved by choosing the added mass and damping coefficients for each wave period, or by applying the MacCamy-Fuchs correction.

The main discrepancies in the second order RAO are for wave periods 8 s and 9 s, which are approximately twice the natural period of the first bending mode. The numerical simulations greatly overpredict the response at these frequencies, indicating that either the second order wave excitation is overpredicted, or the damping is underpredicted in the simulations, or both. The second order wave excitation according to Morison's equation with second order wave kinematics is expected to be overpredicted [44,9]. There may additionally be a change in the hydrodynamic damping in waves compared to the damping in still water which was estimated from the decay tests, but this effect is expected to be minor compared to the overprediction of the loads. Numerical models a_1 and a_2, which include some advective terms, show slightly larger overestimation than model a_3.

Similarly, the third order response is not captured accurately for wave periods close to three times the first natural period of the structure. The uncertainty based on the simplified method is seen to be relatively large for the shortest periods, which is intuitively related to the fact that these waves and the corresponding higher order bending moments are quite small, and become difficult to measure experimentally. The SIMA approach for estimating uncertainty gives larger uncertainty in the second harmonic at 8 s and in the third harmonic at 12 and 14 s, which is related to the excitation of the first mode of the structure.

Fig. 18 shows an example time series of the regular wave elevation and the mudline bending moment. The selected case with $T = 12$ s shows good agreement in the first and second order responses, while

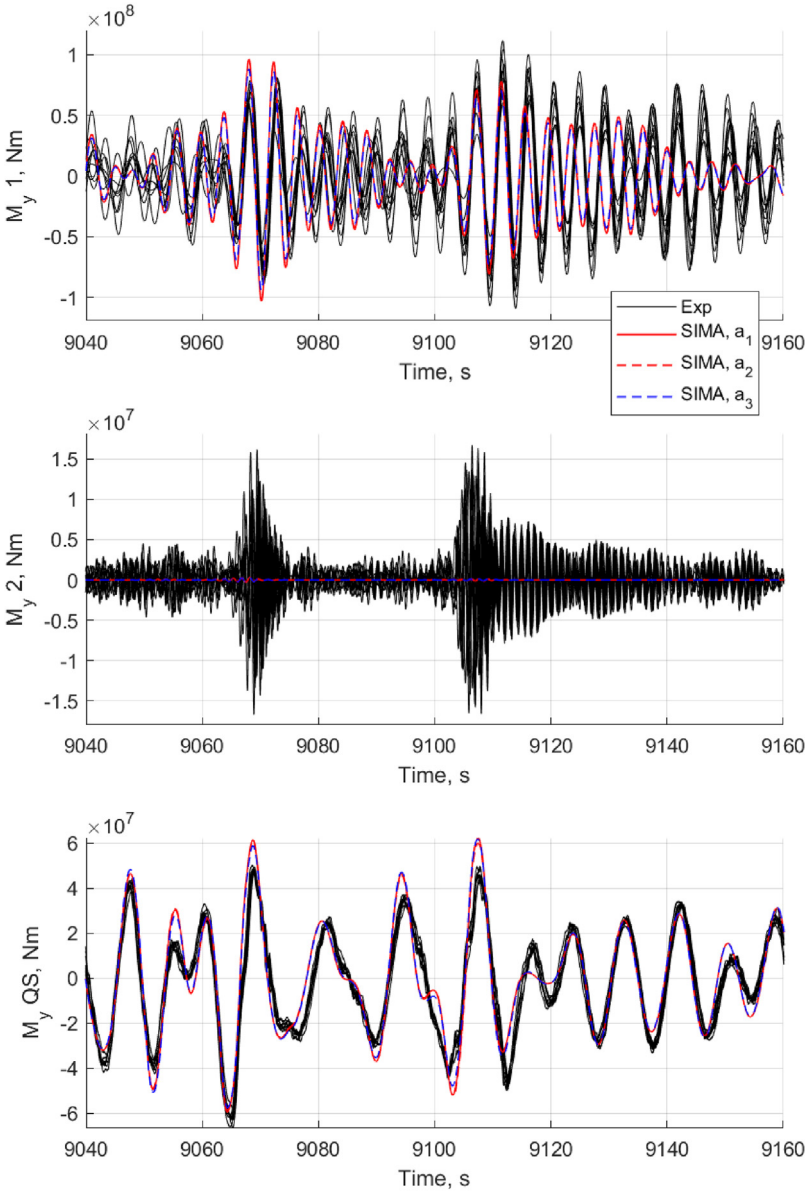

Fig. 23. Comparison of time series of mudline bending moment, bandpass filtered about 1st eigenfrequency (top), 2nd eigenfrequency (middle), and remainder (bottom). H_s = 9 m and T_p = 12.3 s. Repetition tests are included in the experimental results.

the third order component is somewhat overestimated by the numerical results. Even higher frequency components can be seen in the experimental results.

5.4. Long-crested irregular wave tests

Fig. 19 compares the experimental and numerical prediction of the second response metric, the 90th percentile 30-minute bending moment response at $z = -28.5$ m for long-crested waves with $H_s = 9$ m and $T_p = 12.3$ s (TMA spectrum). In Fig. 19, the metric is calculated based on each of the experimental realizations, and also numerically using the corresponding calibrated wave as input. For the first realization, two repetition tests were carried out for the wave calibration, and each measured calibrated wave was used as input to the numerical simulations with the three different acceleration formulations, such that nine numerical results are present for the first realization.

As shown in Fig. 19, the numerical simulations can sometimes, but not always, predict the 90th percentile mudline bending moment within the estimated experimental uncertainty. The estimated uncertainty is very similar for the simplified and SIMA methods. Model a_1 consistently predicts the largest extreme, followed by model a_2, followed by model a_3.

For realization 3, the discrepancy between simulated and predicted results is particularly large. This discrepancy is related to two wave events where the simulation tool, regardless of the acceleration formulation, greatly overpredicts the response at the first bending mode. One of these events in shown in Fig. 20. The simulation tool overpredicts the response to the first of two waves, such that the numerical model still has a significant resonant response when the second wave excites the model even more. This can be seen more clearly in Fig. 21, where the response is bandpass-filtered about the first eigenfrequency, and then about the second eigenfrequency. The rest of the response is then denoted “QS”, although this response includes both the quasi-static contributions and all other contributions outside of the two first natural frequencies (as in [20]). The overprediction of second order wave loads may be a reason for large first mode response to the first wave.

Additional examples of the time series of response are compared in

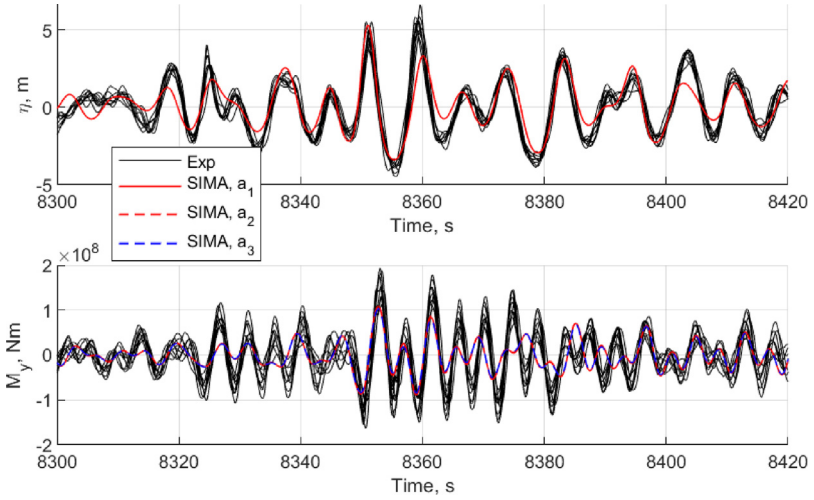

Fig. 24. Comparison of time series of wave elevation (next to the model, with model present) and mudline bending moment, $H_s = 9$ m and $T_p = 12.3$ s, showing poor match for ringing event. Repetition tests are included in the experimental results.

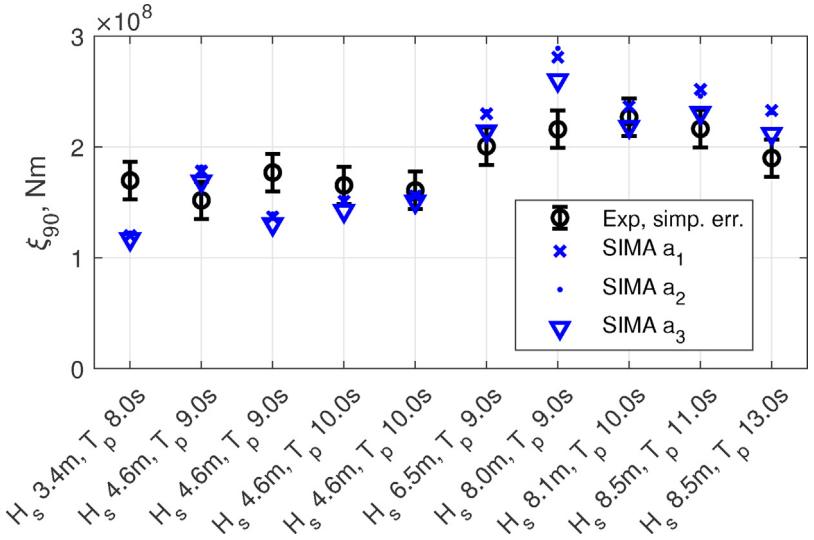

Fig. 25. Comparison of numerical and experimental 90th percentile 30-minute bending moment response at $z = -28.5$ m for various long-crested waves. Results for four independent realizations (seeds) are shown for H_s 4.6 m, T_p 9 s.

Figs. 22–24 . Fig. 22 shows an example of fairly good agreement between the model tests and the numerical model for two maxima. The simulation does not capture the decay of the response at the first natural frequency, but both maxima are captured within the level of variation seen in the repetition tests.

Fig. 23 shows the filtered responses for the same event as in Fig. 22. Here, we can observe that the good agreement in the total response does not necessarily correspond to good agreement in all frequency components. For the first maximum (around 9070 s), the numerical model captures both the first mode and quasi-static contributions fairly well. For the second maximum (around 9110 s), the numerical model overestimates the quasi-static component and underestimates the first mode response. As expected, the numerical model does not have any significant forcing near the second eigenfrequency, and therefore cannot capture any of the response in that frequency range.

Fig. 24 shows the same event as in Fig. 6, and the numerical model is seen to underestimate the bending moment, giving results well below the range of results obtained through repetition tests. The numerical model consistently underpredicts the response following a smaller wave (near 8325 s), possibly due to wave breaking (based on the very sharp elevation pattern), and continues to underpredict the response to the larger waves around 8350 s. The elevation of the wave which excites the response appears to be well captured by the second order approximation, while several other waves in the same portion of the time series are not.

These time series highlight the challenges of drawing event-based conclusions for this very lightly damped model: the response is dominated by the first mode, and the dynamics of the system prior to a subsequent steep wave can be important for the response. While there is significant spread among the experimental repetitions, there are clearly events which this simple numerical model is able to capture within that level of variation.

The 90th percentile 30-minute bending moment response at $z = -28.5$ m was also estimated for additional long-crested wave conditions, as shown in Fig. 25. The repeatability was assumed to be the same as in the $H_s = 9$ m and $T_p = 12.3$ s when assessing the experimental uncertainty using the simplified model. It should be noted that not all of the conditions in Fig. 25 represent 50-year conditions; the 90th percentile 30-minute response is used as a comparison measure but does not have any design relevance. A similar level of agreement is seen for these sea states as in the previously discussed results.

6. Conclusions

Model tests of a fully flexible monopile were carried out at SINTEF Ocean. The level of uncertainty in the model tests has been examined and an engineering model based on a modified Morison's equation with second order wave kinematics has been compared to the experimental results, focusing particularly on a set of response metrics for which experimental uncertainty was estimated.

The experimental results highlighted the resonant response of the monopile when subjected to severe wave loads. The first mode of the response, which could be excited primarily by second and third order wave loads, dominated the response due to the low damping in the system. As expected, the steep wave conditions gave large bending moments at the mudline. Out of the tested sea states, the condition with $H_s = 8.1$ m and $T_p = 10$ s gave the largest measured responses, but the 90th percentile 30 minute bending moment was similar for all of the selected conditions along the 50-year contour with $H_s > 8.0$ m and 9 s $< = T_p < = 12.3$ s.

The uncertainty analysis suggests that the random errors (estimated through repetition tests) are of minor importance compared to bias errors (estimated through a simplified analytical uncertainty propagation and through numerical simulations) for the estimation of RAOs and statistical results. Based on a somewhat conservative estimate - local variation applied as a global variation - the mass and stiffness of the model itself were found to be important contributors to the bias error. The wave elevation and model diameter, where the bias errors were estimated more realistically, were also seen to be important.

The numerical results for the engineering model, considering three formulations of the wave particle acceleration, showed that only some of the response metrics were in agreement within the level of experimental uncertainty. The numerical results including the advective terms of the acceleration always predicted larger responses than the numerical results without these terms. The reasons for discrepancies between numerical and experimetnal results could include the over-prediction of second order wave excitation in the numerical model, incorrect estimation of the third order wave excitation, small differences in the natural period, and the challenges associated with the extremely low damping in the physical model. Due to the low damping of the model, the history of the response was very important for the response in the largest waves. Future work should examine the use of more accurate wave kinematics and higher order wave load formulations for the long-crested and short-crested wave conditions, and new experimental campaigns with additional sources of damping should be considered.

Acknowledgments

The authors gratefully acknowledge the funding provided by the Norwegian Research Council and industry partners through the NOWITECH program (NFR 193823). Mr. Pratim Patel assisted in the analysis of numerical and experimental data.

References

[1] Wind Europe, The European offshore wind industry - key trends and statistics 2016, Tech. rep., Wind Europe (2017). URL https://windeurope.org/wp-content/uploads/files/about-wind/statistics/WindEurope-Annual-Offshore-Statistics-2016.pdf.
[2] O.M. Faltinsen, J.N. Newman, T. Vinje, Nonlinear wave loads on a slender vertical cylinder, J. Fluid Mech. 289 (1995) 179–198, https://doi.org/10.1017/S0022112095001297.
[3] J.N. Newman, Waves and nonlinear processes in hydrodynamics, Kluwer, 1996, pp. 91–102 Ch. Nonlinear scattering of long waves by a vertical cylinder.
[4] S. Malenica, B. Molin, Third-harmonic wave diffraction by a vertical cylinder, J. Fluid Mech. 302 (1995) 203–229.
[5] J. Grue, G. Bjørshol, Ø. Strand, Higher harmonic wave exciting forces on a vertical cylinder, Tech. rep., Preprint Series, Matematisk Institutt Oslo, 1993.
[6] R.C.T. Rainey, Slender-body expressions for the wave load on offshore structures, Proceedings: Math. Phys. Sci. 450 (1995) 391–416.
[7] Y.M. Scolan, B. Molin, G. Deleuil, D. Martigny, Experimental and numerical modelling of the high frequency resonant motion of a vertical cylinder in irregular waves, in: Proceedings of the 15th International Conference on Offshore Mechanics and Arctic Engineering (OMAE1996), Vol. I (1996) 389–396.
[8] C.T. Stansberg, Comparing ringing loads from experiments with cylinders of different diameters - an empirical study, in: 8th International Conference on the Behaviour of Off-Shore Structures (BOSS'97)), Vol. 2 (1997) 95–112.
[9] E.E. Bachynski, T. Kristiansen, M. Thys, Experimental and numerical investigations of monopile ringing in irregular finite-depth water waves, Appl. Ocean Res. 68 (2017) 154–170, https://doi.org/10.1016/j.apor.2017.08.011.
[10] S. Schløer, H. Bredmose, H.B. Bingham, The influence of fully nonlinear wave forces on aero-hydro-elastic calculations of monopile wind turbines, Marine Structures 50 (2016) 162–188.
[11] A.W. Nielsen, F. Schlütter, J.V.T. Sørensen, H. Bredmose, Wave loads on a monopile in 3D waves, in: ASME 2012 31st International Conference on Ocean, Offshore and Arctic Engineering, no. OMAE2012-83533 (2013).
[12] B.T. Paulsen, H. Bredmose, H.B. Bingham, S. Schløer, Steep wave loads from irregular waves on an offshore wind turbine foundation: computation and experiment, in: 32nd International Conference on Ocean, Offshore and Arctic Engineering, no. OMAE2013-10727 (2013).
[13] DNVGL, DNVGL-ST-0437: Loads and site conditions for wind turbines, Tech. rep., DNVGL (2016).
[14] T. Kristiansen, O.M. Faltinsen, Higher harmonic wave loads on a vertical cylinder in finite water depth, J. Fluid Mech. 833 (2017) 773–805.
[15] J. Wienke, H. Oumeraci, Breaking wave impact force on a vertical and inclined slender pile - theoretical and large-scale model investigations, Coastal Eng. 52 (2005) 435–462.
[16] L. de Vos, P. Frigaard, J. de Rouck, Wave run-up on cylindrical and cone shaped foundations for offshore wind turbines, Coastal Eng. 54 (2007) 17–29.
[17] J. Zang, P.H. Taylor, G. Morgan, R. Stringer, J. Orszaghova, J. Grice, M. Tello, Steep wave and breaking wave impact on offshore wind turbine foundations - ringing revisited, in: International Workshop on Water Waves and Floating Bodies (IWWWFB25) (2010).
[18] B.H. Riise, J. Grue, A. Jensen, T.B. Johannessen, High frequency resonant response of a monopile in irregular deep water waves, J. Fluid Mech. 853 (2018) 564–586, https://doi.org/10.1017/jfm.2018.499.
[19] E.J. de Ridder, P. Aalberts, J. van den Berg, B. Buchner, J. Peeringa, The dynamic response of an offshore wind turbine with realistic flexibility to breaking wave impact, in: ASME 2011 30th International Conference on Ocean, Offshore and Arctic Engineering, no. OMAE2011-49563 (2011).
[20] L. Suja-Thauvin, J.R. Krokstad, E.E. Bachynski, E.-J. de Ridder, Experimental results of a multimode monopile offshore wind turbine foundation subjected to steep and breaking irregular waves, Ocean Eng. 146 (2017) 339–351, https://doi.org/10.1016/j.oceaneng.2017.09.024.
[21] A.N. Robertson, Uncertainty analysis of OC5-DeepCwind floating semisubmersible offshore wind test campaign, in: Proceedings of the Twenty-seventh (2017) International Ocean and Polar Engineering Conference, Vol. I (2017) 482–489.
[22] J. Jonkman, S. Butterfield, W. Musial, G. Scott, Definition of a 5-MW reference wind turbine for offshore system development, Tech. Rep. NREL/TP-500-38060, National Renewable Energy Laboratory (February 2009) (2009).
[23] J. Jonkman, Definition of the floating system for Phase IV of OC3, Tech. Rep. NREL/TLP-500-47535, (2010).
[24] J. Jonkman, W. Musial, Offshore code comparison collaboration (OC3) for IEA Wind Task 23 offshore wind technology and deployment, Tech. Rep. NREL/TP-5000-48191, National Renewable Energy Laboratory (2010).
[25] E.-M. Lourens, Force identification in structural dynamics, (2012).
[26] T. Sarpkaya, M. Isaacson, Mechanics of wave forces on offshore structures, Van Nostrand Reinhold, 1981.
[27] Det Norske Veritas, Environmental conditions and environmental loads, Tech. Rep. DNV-RP-C205 (October 2010).
[28] Det Norske Veritas, Design of offshore wind turbine structures, Tech. Rep. DNV-OS-J101 (2007).
[29] C.T. Stansberg, Characteristics of steep second-order random waves in finite and shallow water, in: Proceedings of the ASME 30th International Conference on Ocean, Offshore and Arctic Engineering OMAE2011, Rotterdam, The Netherlands, 2011.
[30] R.G. Dean, R.A. Dalrymple, Water Wave Mechanics for Engineers and Scientists, World Scientific, 1991.
[31] W. Manners, C. Rainey, Hydrodynamic forces on fixed submerged cylinders, in: Proceedings of the Royal Society of London A, Vol. 436 (1992) 13–32.
[32] J. Grue, J. Kolaas, A. Jensen, Velocity fields in breaking-limited waves on finite depth, Eur. J. Mech. - B/Fluids 47 (2014) 97–107.
[33] E. Bouws, H. Günther, W. Rosenthal, C.L. Vincent, Similarity of the wind wave spectrum in finite depth water: 1. spectral form, J. Geophys. Res.: Oceans 90 (C1) (1985) 975–986, https://doi.org/10.1029/JC090iC01p00975.
[34] W.L. Oberkampf, S.M. DeLand, B.M. Rutherford, K.V. Die, Error and uncertainty in modeling and simulation, Reliabil. Eng. System Saf. 75 (2002) 333–357.
[35] R.G. Hills, D.C. Maniaci, J.W. Naughton, V&V framework, Tech. Rep. SAND2015-7455, Sandia National Laboratories, 2015.
[36] ISO/IEC, Uncertainty of measurement - part 3: Guide to the expression of uncertainty in measurement (GUM: 1995), Tech. Rep. ISO/IEC GUIDE 98:3:2008(E), International Organization for Standardization and International Electrical Commission (2008).
[37] R.S. Figliola, D.E. Beasley, Theory and Design for Mechanical Measurements, Wiley, 2006.
[38] A. Naess, T. Moan, Stochastic Dynamics of Marine Structures, Cambridge University

Press, 2013.
[39] C.T. Stansberg, O.T. Gudmestad, S.K. Haver, Kinematics under extreme waves, J. Offshore Mech. Arctic Eng. 130 (2) (2008) 021010, https://doi.org/10.1115/1.2904585.
[40] G.K. Batchelor, An Introduction to Fluid Dynamics, Cambridge University Press, Cambridge, 1970.
[41] M. Damgaard, J.K. Andersen, L.B. Ibsen, L.V. Andersen, Natural frequency and damping estimation of an offshore wind turbine structure, in: Proceedings of the Twenty-second (2012) International Offshore and Polar Engineering Conference (2012) 300–307.
[42] M. Damgaard, L. Ibsen, L. Andersen, J. Andersen, Cross-wind modal properties of offshore wind turbines identified by full scale testing, J. Wind Eng. Ind. Aerodyn. 116 (2013) 94–108, https://doi.org/10.1016/j.jweia.2013.03.003.
[43] R. Shirzadeh, W. Weijtjens, P. Guillaume, C. Devriendt, The dynamics of an offshore wind turbine in parked conditions: a comparison between simulations and measurements, Wind Energy 18 (10) (2014) 1685–1702 arXiv:https://onlinelibrary.wiley.com/doi/pdf/10.1002/we.1781, doi:10.1002/we.1781. URL https://onlinelibrary.wiley.com/doi/abs/10.1002/we.1781.
[44] J. Krokstad, C. Stansberg, A. Nestegård, T. Marthinsen, A new nonslender ringing load approach verified against experiments, Trans. ASME J. Offshore Mech. Arctic Eng. 120 (1) (1998) 20–29.